

# The Complex Hodological Architecture of the Macaque Dorsal Intraparietal Areas as Emerging from Neural Tracers and DW-MRI Tractography

<https://doi.org/10.1523/ENEURO.0102-21.2021>

**Cite as:** eNeuro 2021; 10.1523/ENEURO.0102-21.2021

Received: 15 March 2021

Revised: 21 April 2021

Accepted: 1 May 2021

---

*This Early Release article has been peer-reviewed and accepted, but has not been through the composition and copyediting processes. The final version may differ slightly in style or formatting and will contain links to any extended data.*

**Alerts:** Sign up at [www.eneuro.org/alerts](http://www.eneuro.org/alerts) to receive customized email alerts when the fully formatted version of this article is published.

Copyright © 2021 Caminiti et al.

This is an open-access article distributed under the terms of the Creative Commons Attribution 4.0 International license, which permits unrestricted use, distribution and reproduction in any medium provided that the original work is properly attributed.

1     **The Complex Hodological Architecture of the Macaque Dorsal Intraparietal**  
2             **Areas as Emerging from Neural Tracers and DW-MRI Tractography**

3  
4     **Abbreviated Title:** *Connections of Dorsal Intraparietal Areas*  
5

6     **Roberto Caminiti**<sup>1</sup>, **Gabriel Girard**<sup>2,3,4</sup>, **Alexandra Battaglia-Mayer**<sup>5</sup>, **Elena Borra**<sup>6</sup>, **Andrea**  
7     **Schito**<sup>5,7</sup>, **Giorgio M. Innocenti**<sup>8,9</sup>, **Giuseppe Luppino**<sup>6</sup>  
8

9     <sup>1</sup> Neuroscience and Behavior Laboratory, Istituto Italiano di Tecnologia (IIT), 00161 Rome,  
10     Italy, <sup>2</sup>CIBM Center for Biomedical Imaging, EPFL, CH-1015, Lausanne, Switzerland, <sup>3</sup> Radiology  
11     Department, Centre Hospitalier Universitaire Vaudois and University of Lausanne, CH-1011,  
12     Lausanne, Switzerland, <sup>4</sup>Signal Processing Laboratory (LTS5), École Polytechnique Fédérale de  
13     Lausanne, CH-1015, Lausanne, Switzerland, <sup>5</sup>Department of Physiology and Pharmacology,  
14     University of Rome SAPIENZA, 00185 Rome, Italy, <sup>6</sup>Università di Parma, Dipartimento di  
15     Medicina e Chirurgia, 43125 Parma, Italy, <sup>7</sup>PhD Program in Behavioral Neuroscience,  
16     University of Rome SAPIENZA, 00185 Rome, Italy, <sup>8</sup>Department of Neuroscience, Karolinska  
17     Institutet, 171 1777 Stockholm, Sweden, <sup>9</sup>Brain and Mind Institute, Swiss Federal Institute of  
18     Technology Lausanne (EPFL), Lausanne, Switzerland.  
19

20     **Author Contributions:** RC, ABM, EB, GMI and GL, Designed Research; RC, GG, ABM, EB, AS and  
21     GL, Performed Research; GG, EB, ABM, AS, GL Analysed data; RC, GG, ABM, EB and GL Wrote the  
22     paper

23     **Corresponding author email address:** [roberto.caminiti@uniroma1.it](mailto:roberto.caminiti@uniroma1.it)  
24

25     **Number of pages (including page with table):** 38

26     **Number of figures:** 12

27     **Number of tables:** 1

28     **Number of words:**

29             Abstract: 159

30             Significant Statement: 120

31             Introduction: 689

32             Discussion: 1569  
33

34     **Conflict of interest statement:** The authors declare no competing financial interests

35     **Acknowledgments:** We acknowledge the support of the Istituto Italiano di Tecnologia to R.C.  
36     and the access to the facilities and expertise of the CIBM Center for Biomedical Imaging,  
37     founded and supported by Lausanne University Hospital (CHUV), University of Lausanne  
38     (UNIL), Ecole Polytechnique Fédérale de Lausanne (EPFL), University of Geneva (UNIGE) and  
39     Geneva University Hospitals (HUG). This work was supported by the MIUR of Italy (PRIN 2017  
40     to A.B.M, Grant n. 201794KEER\_002 and PRIN 2017 to E.B, Grant n. 2017KZNZLN\_002).

41     **Dedication:** This paper is dedicated to our co-author and friend Giorgio M. Innocenti, who  
42     passed away unexpectedly on January 12, 2021.  
43

44

45 **Abstract**

46

47 In macaque monkeys, dorsal intraparietal areas are involved in several daily visuo-motor  
48 actions. However, their border and sources of cortical afferents remain loosely defined.49 Combining retrograde histological tracing and MRI diffusion-based tractography we found a  
50 complex hodology of the dorsal bank of the IPS, which can be subdivided into a rostral area51 PEip, projecting to the spinal cord, and a caudal area MIP lacking such projections. Both  
52 include a rostral and a caudal sector, emerging from their ipsilateral, gradient-like53 connectivity profiles. As tractography estimations, we used the cross-sectional volume of the  
54 white matter bundles connecting each area with other parietal and frontal regions, after55 selecting ROIs corresponding to the injection sites of neural tracers. For most connections,  
56 we found a significant correlation between the proportions of cells projecting to all sectors57 of PEip and MIP along the continuum of the dorsal bank of the IPS and tractography. The  
58 latter also revealed “false positive” but plausible streamlines awaiting histological validation.

59

60 **Significance Statement**

61

62 Combined histological and DW-MRI tractography revealed that intraparietal areas PEip and  
63 MIP share common inputs from other parietal, frontal and, to a lesser extent, cingulate64 areas, although with different gradient-like connectivity profiles. Both tractography and  
65 histology revealed a high number of common paths, although tractography showed false66 positive connections awaiting histological validation. A correlation was performed between  
67 the proportion of labelled cells projecting to PEip and MIP and the diffusion-based68 connectivity estimation of the regions of interest corresponding to the injection sites of  
69 retrograde tracers. The results showed a significant correlation from most connections70 studied, opening a window for future studies contrasting proportions of cells giving rise to  
71 the fiber bundles connecting cortical areas with measures of diffusion tractography

72 connectivity.

73

74 **INTRODUCTION**

75 Areas PEip (PE intraparietal) and MIP (medial intraparietal) in the dorsal bank of the  
76 intraparietal sulcus (db-IPS) of monkeys are two crucial nodes for controlling visuomotor  
77 behavior. This view stems from different sources of information. The first relates to their  
78 input-output relationships (Johnson et al., 1996; Caminiti et al., 1996; Matelli et al., 1998;  
79 Marconi et al., 2001; Bakola et al., 2017; Battaglia-Mayer and Caminiti, 2019), since they  
80 receive projections from visuomotor areas V6A and PGm and project to premotor and motor  
81 cortex (see Caminiti et al., 2017). The second consists in the functional properties of their  
82 neurons (see Lacquaniti et al., 1995; Johnson et al., 1996; Batista et al., 1999), which  
83 combine retinal signals about target location, with eye and hand position and movement  
84 signals within their directional tuning fields (Battaglia-Mayer et al., 2000, 2001). The third  
85 stems from the consequences of lesions of parieto-occipital areas in humans, consisting in a  
86 defective visual control of reaching, known as optic ataxia (Bálint, 1909; see Rossetti and  
87 Pisella, 2018).

88 To date, aspects of PEip and MIP connectivity remain unknown, since the difficulty of  
89 injecting of histological tracers over the entire dorso-ventral extent of the IPS rendered only  
90 a partial view of its connectivity. Previous attempts to mark the PEip/MIP border were based  
91 on the presence of cortico-spinal projections (Matelli et al., 1998) or on myeloarchitectonic  
92 criteria (Bakola et al., 2017). Based on cytoarchitectonics, Pandya and Seltzer (1982) labelled  
93 this region of the superior parietal lobule (SPL) as area PEa, to distinguish it from the  
94 remaining part of area 5. This study was, however, antecedent to the identification of the  
95 medial intraparietal area (MIP), as the dorsal intraparietal region projecting to area PO  
96 (Colby et al., 1988).

97  
98 The difficulties of histological studies can tentatively be overcome by diffusion-weighted MRI  
99 tractography (DW-MRI). Albeit known limitations, such as the identification of false-positive  
100 connections and biases toward reconstructing short and strong connections (Jones et al.,  
101 2013; Van Essen et al., 2014; Jbabdi et al., 2015; Knosche et al., 2015; Jeurissen et al., 2017;  
102 Maier-Hein et al., 2017; Aydogan et al., 2018; Schilling et al., 2019a,b; Girard et al., 2020),  
103 tractography shows promising results when compared to histology (Dauguet et al., 2007;  
104 Dyrby et al., 2007; Seehaus et al., 2012; Jbabdi et al., 2013; Thomas et al., 2014; Azadbakht  
105 et al., 2015; Calabrese et al., 2015; Gyengesi et al., 2015; van den Heuvel et al., 2015;

106 Knosche et al., 2015; Donahue et al., 2016; Delettre et al., 2019; Ambrosen et al., 2020;  
107 Girard et al., 2020). Particularly, Calabrese et al. (2015), Donahue et al. (2016) and Ambrosen  
108 et al. (2020) have reported positive results when comparing labelled cells count from tracer  
109 injections in the monkey brain with connectivity weights derived from DW-MRI  
110 tractography.

111 In this study, we combined tractography and histology to elucidate the connectivity of PEip  
112 and MIP. In two macaque monkeys, we injected different retrograde fluorescent tracers  
113 along the antero-posterior (A-P) extent of the db-IPS and established their putative border  
114 based on the distribution of cortico-spinal cells projecting to the cervical segments of the  
115 spinal cord, as determined in two other animals (see Matelli et al., 1998). The connectivity  
116 of the db-IPS was studied with tractography in a fifth animal and compared in a quantitative  
117 fashion with histological data. To explore potential connections of PEip and MIP not yet  
118 revealed by tract tracing studies, the dorso-ventral extent of these areas was subdivided into  
119 different regions of interest (ROIs). This was inspired by earlier anatomo-functional studies  
120 (Johnson et al., 1996; Battaglia-Mayer et al., 2001) showing systematic changes of both  
121 functional properties and cortico-cortical connectivity in the dorso-ventral extent of the  
122 intraparietal cortex.

123 Combining histology and tractography revealed a significant correlation between the  
124 proportion of cells projecting to MIP and/or PEip and the diffusion-based connectivity  
125 estimates of the corresponding streamlines. Furthermore, tractography resulted to be very  
126 useful in revealing aspects of the db-IPS connectivity which could not be explored based on  
127 neural tracer injections. Beyond advancing the information about the connectivity of the IPS,  
128 these results offer a quantitative cross-validation of the two methods and call for a  
129 histological validation of predictions emerging from tractography.

130

131

## 132 **MATERIAL AND METHODS**

### 133 **Neural tracer experiments**

134

135 **Subjects.** The tracer experiments were carried out in four male monkeys. In two animals  
136 (*Macaca mulatta*; Cases 72 and 73; body weight 12 kg and 12.50 Kg, respectively) retrograde  
137 neural tracers were injected at different antero-posterior (A-P) levels of the db-IPS.

138 Additional data from two *Macaca nemestrina* (Cases 10 and 21; body weight 5.2 and 4.4 Kg,  
139 respectively), in which a retrograde tracer was injected in the lateral funiculus of the spinal  
140 cord, were used for visualizing the origin of corticospinal projections from the db-IPS. Data  
141 from these two cases have been already partially used in previous studies (Luppino et al.,  
142 1994; Matelli et al., 1998; Rozzi et al., 2006; Borra et al., 2010).

143 Animal handling as well as surgical and experimental procedures complied with the  
144 European law on the humane care and use of laboratory animals (Directives 86/609/EEC,  
145 2003/65/CE, and 2010/63/EU) and Italian laws in force regarding the care and use of  
146 laboratory animals (D.L. 116/92 and 26/2014). All procedures were approved by the  
147 Veterinarian Animal Care and Use Committee of the University of Rome SAPIENZA or of the  
148 University of Parma, and then authorized by the Italian Ministry of Health.

149

150 **Surgical procedures.** Surgery was performed under aseptic conditions. Cases 72 and 73 were  
151 pre-anaesthetized with ketamine (5 mg/kg, *i.m.*) and dexmedetomidine hydrochloride (0.1  
152 mg/kg; *i.m.*), intubated and anaesthetized with a mix of Oxygen/Isoflurane (1-3% to effect).  
153 Lidocaine (2%) was used locally to minimize pain during skin incision in the scalp.  
154 Desametasone (6mg/kg) was given before dura opening, to prevent brain inflammation and  
155 edema. The skull was then trephined over the target region, and the dura was opened to  
156 expose the intraparietal sulcus. A constant infusion of Fentanil (0.2mg/kg/h; *i.v.*) was  
157 performed until the end of the surgical procedures. The selection of the injection sites was  
158 based on identified anatomical landmarks, such as the rostral tip of the IPS. In Cases 10 and  
159 21 in which tracers were injected in the spinal cord, under general anesthesia (Ketamine, 5  
160 mg/kg *i.m.* and Medetomidine, 0.08–0.1mg/kg *i.m.*), following a laminectomy, the dura was  
161 opened, and the segment of the spinal cord selected for the injection exposed. During all  
162 surgeries, hydration was maintained with saline, and temperature using a heating pad. Heart  
163 rate, blood pressure, respiratory depth, O<sub>2</sub> saturation, and body temperature were  
164 continuously monitored.

165

166 **Tracer injections.** Once the appropriate site was chosen, fluorescent tracers (Fast Blue [FB]  
167 3% in distilled water, Diamidino Yellow [DY] 2% in 0.2 M phosphate buffer at pH 7.2, both  
168 from Dr. Illing Plastics GmbH, Breuberg, Germany) were slowly pressure injected with a glass  
169 micropipette attached to the needle of a Hamilton microsyringe at different depths and A-P

170 levels in the medial bank of the IPS. In Case 72 (Fig. 1), FB (two deposits, 0.15  $\mu$ l each, at a  
171 depth of 3 and 4 mm, in the anterior part of area MIP, aMIP) and DY (two deposits, 0.15  $\mu$ l  
172 each, at a depth of 3 and 4 mm, in the posterior part of area PEip, pPEip) were injected at  
173 about 16 and 13 mm caudal to the rostral end of the right IPS, respectively. In Case 73 (Fig.  
174 1), FB (0.3  $\mu$ l) and DY (0.3  $\mu$ l) were injected at a depth of 4 mm, caudal to the rostral end of  
175 the left IPS, at about 8,5 mm (in the anterior part of area PEip, aPEip) and 18 mm, (in the  
176 posterior part of area MIP, pMIP), respectively. To facilitate comparison of the data with  
177 Case 72, the brain in Case 73 is shown as a right hemisphere. After the tracer injections were  
178 placed, the dura flap was sutured, the bone was replaced, and the superficial tissues were  
179 sutured in layers.

180 In Cases 10 and 21 the retrograde tracer horseradish peroxidase (HRP, 30% in 2%  
181 lysolecithin, Sigma-Aldrich, St. Louis, MO) was, then, pressure injected with a 5  $\mu$ l Hamilton  
182 microsyringe in the left lateral funiculus in both monkeys (Fig. 2). In one animal (Case 10) the  
183 tracer (multiple injections, total amount 10  $\mu$ l) was injected at the C4-C5 spinal level, in the  
184 other (Case 21, multiple injections, total amount 15  $\mu$ l) at C3--C5 level. Upon the completion  
185 of the injections, the spinal cord was covered with Gelfoam and wounds were closed in  
186 layers.

187 Upon recovery from anesthesia, the animals were returned to their home cages and closely  
188 monitored. Dexamethasone and prophylactic broad-spectrum antibiotics were administered  
189 pre- and postoperatively. Furthermore, analgesics were administered intra- and  
190 postoperatively. Figure 1 summarizes the locations of the injections, the injected tracers.

### 191 ***Histological procedures***

192 At the end of the survival time (26 days for Case 72; 23 days for Case 73; 3 days for Cases 10  
193 and 21), the animals were given a dose of atropine (0.4 ml; i.m.) and diazepam (Valium, 2ml;  
194 i.m.), pre-anaesthetized as above, and received an intravenous lethal injection of sodium  
195 thiopental (200 mg/kg; i.v). They were perfused through the left cardiac ventricle with saline,  
196 4% paraformaldehyde, and 5% glycerol in this order. All solutions were prepared in  
197 phosphate buffer 0.1 M, pH 7.4. Each brain was then blocked coronally on a stereotaxic  
198 apparatus, removed from the skull, photographed, and placed in 10% buffered glycerol for 3  
199 days and 20% buffered glycerol for 4 days. Finally, each brain was cut frozen in coronal  
200 sections 60  $\mu$ m thick. In Cases 10 and 21 the spinal cord was cut in 60  $\mu$ m thick coronal  
201 sections. In Cases 72 and 73, one series of every fifth section was mounted, air-dried, and

202 quickly cover-slipped for fluorescence microscopy. In Cases 10 and 21, one series of every  
203 fifth section through the right hemisphere and the brainstem, and every tenth section  
204 through the spinal cord was processed for HRP histochemistry using tetramethylbenzidine as  
205 the chromogen (Mesulam, 1982). Sections were rinsed in 0.01 M acetate buffer, pH 3.3, and  
206 developed at 4°C in a solution of 0.09% sodium nitroferricyanide, 0.005%  
207 tetramethylbenzidine, and 0.006% hydrogen peroxide in 0.01 M acetate buffer. Finally, one  
208 series of every fifth section in all brains and of every tenth section in the spinal cord in Cases  
209 10 and 21, was stained with the Nissl method (0.1% thionin in 0.1M acetate buffer, pH 3.7).

#### 210 ***Injection sites and distribution of retrogradely labelled neurons.***

211 In Cases 72 and 73, the FB and DY injection sites, defined according to Kuypers and Huisman  
212 (1984) and Conde´ (1987), were completely restricted to the cortical gray matter, involving  
213 almost the entire cortical thickness, or at least layers III–V. Injection sites were then  
214 attributed to area PEip or MIP, as defined from the distribution of corticospinal labelled  
215 neurons in the db-IPS (Cases 10 and 21), as detailed in Table 1.

216 The cortical distribution of FB- and DY-retrogradely labelled cells (Cases 72 and 73), as well  
217 as of HRP-labelled cells (Cases 10 and 21), here referred to as RLC (retrogradely-labelled  
218 cells), was plotted in sections every 600 µm (300 µm in Cases 10 and 21). In each examined  
219 section the outer and inner cortical borders and the location of each labelled neuron were  
220 plotted with the aid of inductive displacement transducers mounted on the X and Y axes of  
221 the microscope stage. The transducer signals were digitized and stored by using software  
222 developed in our laboratory that allows the visualization of section outlines, of grey-white  
223 matter borders, and of labelled cells.

224 Data from individual sections were then imported into the 3-dimensional (3D)  
225 reconstruction software developed in house (Demelio et al., 2001) to create volumetric  
226 reconstructions of the hemispheres from individual histological sections containing  
227 connectional and/or architectonic data and providing realistic visualizations of the labeling  
228 distribution. The distribution of RLC on exposed cortical surfaces was visualized in mesial and  
229 dorsolateral views of the hemispheres, whereas that in the db-IPS in lateral views of the  
230 hemispheres, in which the bank was exposed with dissection of the inferior parietal lobule  
231 and the temporal lobe.

232 The nomenclature and the map adopted for the areal attribution of the labelled neurons was  
233 the same of that used in a recent quantitative study of the connectivity of the parieto-frontal



234 system (Caminiti et al., 2017). Briefly, the superior and medial parietal cortex was defined  
235 according to architectonic criteria described in Pandya and Seltzer (1982) and Luppino et al.  
236 (2005), while area MIP was defined based on the distribution of corticospinal projections  
237 (see Results). In the inferior parietal lobule the gyral convexity areas were defined according  
238 to cyto- and chemoarchitectonic criteria described in Gregoriou et al. (2006) and those of  
239 the lateral bank of the intraparietal sulcus based on connectional criteria described in Borra  
240 et al. (2008). The fundal region of the intraparietal sulcus was assigned to the ventral  
241 intraparietal (VIP) area as defined by Colby and Duhamel (1991). In the frontal lobe, frontal  
242 and cingulate motor areas were defined according to architectonic criteria described in  
243 Matelli et al. (1985, 1991) and Belmalih et al. (2009). Prefrontal areas were defined  
244 according to Carmichael and Price (1994), Gerbella et al. (2007), and Saleem et al. (2014).

245

#### 246 ***Quantitative analysis and laminar distribution of retrograde labeling.***

247 In all the cases, we counted the number of RLC plotted in the ipsilateral hemisphere, beyond  
248 the limits of the injected area, in sections at every 600  $\mu\text{m}$  interval. Cortical afferents to  
249 areas PEip or MIP were then expressed in terms of the percentage of labelled neurons found  
250 in a given cortical subdivision, with respect to the overall retrograde labeling found for each  
251 tracer injection. As for the brain parcellation adopted in this study, for both histological and  
252 tractography data, see dedicated paragraph below.

253 Furthermore, to obtain information about the laminar patterns of the observed connections,  
254 the labeling attributed to a given area and reliably observed across different sections and  
255 cases was analyzed in sections at every 300  $\mu\text{m}$  in terms of amount of RLC located in the  
256 superficial (II–III) versus deep (V–VI) layers.

257

#### 258 **Diffusion-weighted MRI experiment**

##### 259 ***Brain processing for ex-vivo DW-MRI acquisition.***

260 The diffusion-weighted MRI (DW-MRI) data from ex-vivo brain of a male *Macaca mulatta*  
261 (M105, 4 years and 10 months old, 10.1 kg body weight) available from Ambrosen et al.  
262 (2020) was used. The brain was perfused following the protocol illustrated in Ahmed et al.

263 (2012) and prepared for MRI ex-vivo scanning as described by Dyrby et al. (2011). The DW-  
264 MRI data were acquired at 0.5 mm isotropic resolution. The data were sampled in 180  
265 uniformly distributed directions on each of three b-value shells ( $b = [1.477, 4.102, 8.040]$   
266  $\text{ms}/\mu\text{m}^2$ ) and 9 non-diffusion-weighted images ( $b=0 \text{ ms}/\mu\text{m}^2$ ). The protocol was repeated  
267 twice and averaged before further processing (for more details on the MRI acquisition  
268 protocol, see Ambrosen et al. 2020). We also used the midcortical surface from Ambrosen et  
269 al. (2020). The Fiber Orientation Distributions were estimated using the Multi-Shell Multi-  
270 Tissue Constrained Spherical Deconvolution algorithm available in the MRtrix3 software  
271 (Jeurissen et al., 2014; Tournier et al., 2019). The brain partial volume estimates for the  
272 white matter, grey matter, and cerebrospinal fluid were obtained from the averaged non-  
273 diffusion-weighted image using the FSL Fast software (Zhang et al., 2001).

274

275

#### 276 **Brain Parcellation**

277 We used the brain parcellation of the right hemisphere available in Girard et al. (2020). Fifty-  
278 nine cortical areas were manually parcellated following the study by Caminiti et al (2017), on  
279 the animal used for the ex-vivo DW-MRI acquisition. Areas 46dr and 46dc were grouped in a  
280 single region of interest, (ROI) 46d. Similarly, we grouped areas 46vr, r46vc, c46vc in ROI 46v,  
281 areas c12r, i12r, r12r in ROI 12r, areas 9l, 9m in ROI 9, areas 45A, 45B in ROI 45, areas 8Ad,  
282 8Av in ROI 8r&FEF, areas F7PMdr, F7SEF in ROI F7, areas F2vr, F2preCD in ROI F2, areas F5p,  
283 F5a/44, F5c in ROI F5. Areas 24 and 25, the insula and Tpt were added to cortical parcellation  
284 based on atlases of the rhesus monkey brain (Paxinos et al., 2000; Saleem et al., 2012).  
285 Together, these cortical areas make 48 ROIs for investigating the connectivity of PEip and  
286 MIP. To obtain a detailed parcellation of the db-IPS, we first merged area PEip and MIP in a  
287 single area. This resulted in 38 A-P MRI coronal slices (from #105 to #68; each 0.5 mm  
288 thickness) of the db-IPS, which was then divided into three equally wide sectors: dorsal,  
289 middle, and ventral. However, the most anterior part of the area PEip was excluded from the  
290 fine parcellation of the db-IPS, because of the difficulty in identifying three sectors. The  
291 parcellation was done in the native MRI image space. The MRI images were manually aligned  
292 to the stereotaxic plane of the histological sections for visual inspection.

293 ***DW-MRI Tractography and Connectivity***

294 Probabilistic streamline tractography was performed using the Particle Filtering  
295 Tractography algorithms (Girard et al., 2014) available in the DIPY software library  
296 (Garyfallidis et al., 2014). Tractography was initiated in all white matter voxels using 25 seeds  
297 per voxel (9,713,750 seeds). Streamlines with a length superior to 2 mm in the white matter  
298 volume were used as input to the Convex Optimization Modelling for Microstructure  
299 Informed Tractography (COMMIT) method (Daducci et al., 2014). COMMIT was used to  
300 estimate each streamline contribution (weights) to the intra-axonal MRI signal fraction  
301 following the Stick-Zeppelin-Ball white matter microstructure model (Panagiotaki et al.,  
302 2012, Daducci et al., 2014). The tractography and microstructure estimation was repeated  
303 four times, resulting in a total of 23,137,312 streamlines and weights. All streamlines with an  
304 endpoint located in one of the 48 cortical ROIs and an endpoint in the A-P coronal slices of  
305 the db-IPS were selected for the diffusion-based connectivity analysis. Streamlines were  
306 selected using the MRtrix3 *tck2connectome* (Tournier et al., 2019) command, identifying  
307 connected ROIs with a radial search of 1 mm around streamlines endpoints. This resulted in  
308 73,390 streamlines connecting the db-IPS to the cortical areas (dorsal: 29,378; middle:  
309 24,474; ventral: 19,538).

310

311 ***Diffusion-based Connectivity Estimation***

312 To cover a similar extent as the tracer injections, we merged the dorsal and middle sectors  
313 of our three-fold subdivision of the db-IPS. We used a sliding window of five MRI coronal  
314 slice (2.5 mm) moving in the A-P direction selecting all streamlines connecting the merged  
315 sectors of the window to the cortical ROIs. From the 38 coronal MRI slices (#105 to #68), we  
316 obtained 34 windows in the A-P extent of the db-IPS, with each window made of five  
317 consecutive MRI slices (centered at slices #103 to #70, the two bordering slices at each  
318 extremity of the db-IPS were excluded). For each sliding window and each cortical ROI, we  
319 computed the sum of the COMMIT weights (i.e., estimation of the intra-axonal MRI signal  
320 fraction) associated with streamlines interconnecting them.

321 The diffusion-based connectivity distribution of a sliding window (dorsal and middle sectors  
322 of the db-IPS of five consecutive coronal MRI slices) was obtained by dividing each ROI's

323 weight by the sum of the weights associated with streamlines connecting that window to all  
324 cortical ROIs. The Pearson's correlation coefficient was used to compare the diffusion-based  
325 connectivity distribution of each window with the histological cell count distributions of the  
326 four injection sites.

327

328

329

## 330 **RESULTS**

### 331 **Neural Tracers Study**

#### 332 ***Subdivision of the db-IPS and location of the injection sites***

333 The location of the injection sites placed at different A-P levels in the db-IPS and involving  
334 the bank for several mm in depth (cases 72 and 73) is shown in Figure 1. To assign injection  
335 sites and RLC in the db-IPS to specific cortical entities, as in Matelli et al. (1998), we  
336 subdivided this region based on the distribution of corticospinal neurons, which clearly  
337 distinguishes between a rostral and a caudal sector (Fig. 2).

338 The upper part of Figure 2 shows the overall distribution on the dorsolateral cortical surface  
339 of the corticospinal labelled neurons observed after the injection of HRP in the lateral  
340 funiculus at the upper cervical levels (Cases 10 and 21). The extensive labelling observed in  
341 both cases all over the precentral and postcentral gyri, except their most lateral part,  
342 suggested complete, or almost complete involvement of the contralateral lateral funiculus  
343 by the HRP injection. In the lower part of Figure 1, lateral views of the two hemispheres  
344 show the distribution of the RLC observed in the db-IPS. In both hemispheres, the rostral  
345 part of the bank hosted the highest number of them, as compared to its caudal part, from  
346 the crown to the fundus. This rostral sector, which does not appear to project to the  
347 thoraco-lumbar spinal cord (Matelli et al., 1998) and hosts neurons dysynaptically connected  
348 with hand motoneurons (Rathelot et al., 2017), has been here referred to as to PEip,  
349 according to the original definition of Matelli et al. (1998). Caudal to PEip, corticospinal  
350 neurons appeared to be confined to the uppermost part of the bank, which, therefore, for  
351 most of its extent lacked these projections. This last sector as a whole has been here

352 referred to as area MIP. The border between PEip and MIP tended to run obliquely, from a  
353 ventro-rostral to a dorso-caudal position and, at about half of the depth of the bank  
354 appeared to be located at an A-P level of about 13 mm caudal to the rostral end of the IPS. In  
355 the caudalmost part of the bank, MIP borders caudally with V6A (Luppino et al., 2005; Bakola  
356 et al., 2017).

357

### 358 ***Ipsilateral cortical projections to area MIP***

359 Two tracer injections targeted MIP (Fig.1), one in Case 72, where DY was placed in aMIP and  
360 one in Case 73, where FB was delivered in pMIP. The analysis of the distribution of RLC in the  
361 ipsilateral hemisphere revealed substantial labelling in both frontal and parietal areas with a  
362 smaller contribution from selected cingulate zones (Table 1). The results from these two  
363 injections will be described together and are illustrated in Figures 3-5.

364

#### 365 *Projections from frontal and cingulate cortex*

366 In frontal cortex, RLC were found mostly in a region spanning from the ventro-rostral sector  
367 of area F2 (F2vr), around the spur of the arcuate sulcus, up to the border with M1 (primary  
368 motor cortex, F1) in the dorsal part of premotor cortex (Figs. 3, 4:2-4, 5:2-6). In both cases,  
369 they represented about 10% of the total number of RLC. Labelling extended over the  
370 classical arm region described in previous studies that combined anatomical tracing and  
371 physiological recording during reaching tasks (Caminiti et al., 1991; Johnson et al., 1996), as  
372 well as in the region of the arcuate spur, where neural activity is more related to hand  
373 movement (Fogassi et al., 1999). Smaller proportions of RLC (3,7-3,8%; Figs. 4: 4-6 and Fig.  
374 5: 6-11) were found over the arm region of M1 (see Johnson et al., 1996), lateral to the pre-  
375 central dimple. No RLC were found in the mesial part of M1, in the leg and foot  
376 representations, in line with data showing that neural activity in MIP is mostly related to  
377 visuomotor control of coordinated eye-hand actions.

378 A very small proportion of RLC was observed in area F3 (supplementary motor area, SMA;  
379 1,3-1,6%; Fig 3), and a moderate number of them was located in the agranular cingulate area  
380 24c/d (2-2,7% Figs. 4:4-5, 5:4-6) and in the granular cingulate area 23c (1,2-2,3%; Figs. 4:7-8,  
381 5:7-13).

382

383 *Projections from parietal cortex*

384 In PPC, RLC were found in both the superior (SPL) and, to a lesser extent, inferior (IPL)  
385 parietal lobules. In SPL, after the aMIP injection, there was strong labelling in areas PEc  
386 (18,2%; Figs. 3, 4: 14-15), PEip (17,8%; Figs. 4, 5:7-13) and PE (13,8%; Figs. 3, 4: 10-12), After  
387 the pMIP injection, the labelling was similarly robust in PEip (16,5%; Figs. 3, 5:9-13), weaker  
388 but still strong in PEc (12,5%; Figs. 3, 5: 3-16), modest in PE (4,1%).

389 On the medial wall of the SPL, projections from area PEci were stronger to pMIP (12,9%)  
390 than to aMIP (6,1%; Figs. 3, 4:13-14, 5:14-16) and those from PGm were mostly addressed to  
391 aMIP (7,1%; Figs.3, 4: 14). Finally, projections from area V6A were mostly (22.2%) addressed  
392 to pMIP (Fig.5:17-19), but in smaller proportion also to aMIP (7,3%; Fig. 4:16-17).

393 The only IPL areas projecting to MIP, although with a relatively modest proportion of cells  
394 (4,3% to pMIP; 3.65 to aMIP), were areas PG (Figs. 3, 4:11-13, 5:13) and PGop (Fig 4:7-12;  
395 Fig. 5:8-13). RLC were sparse in VIP (Fig.4:7-11), virtually absent in AIP, absent in LIP. Area  
396 MST contained a very small proportion (0,7%) of cells projecting to aMIP. Finally, very few  
397 RLC were observed in SI and SII. No RLC projection to MIP were found in prefrontal areas.

398 ***Ipsilateral cortical projections to area PEip***

399 Two tracer injections targeted PEip (Fig. 1), one in Case 73, where FB resulted to be placed at  
400 about its middle part, and one in Case 72, where DY was placed in the caudalmost part of it,  
401 adjoining the border with MIP (pPEip). As observed after the tracer injections in MIP, RLC  
402 substantially involved frontal and parietal areas, and their distribution reflected A-P  
403 gradients of connectivity in the db-IPS.

404

405 *Projections from frontal and cingulate cortex*

406 As shown in Table 1, after both the aPEip and the pPEip injections robust labelling was found  
407 in M1 (15,6% and 13,5%, respectively). Robust connectivity with M1, therefore, appears to  
408 be a unifying connectional feature of PEip, together with the projection to the spinal cord. In  
409 M1, the labelling was mostly located in the medial bank of the CS, thus involving the “new”  
410 M1 (Rathelot and Strick, 2009), where hand movements are represented (Figs. 4:5-8, 5:5-  
411 10). After the pPEip injection, RLC also extended more rostrally in M1 over the cortex of the  
412 precentral convexity, lateral to the pre-central dimple (pre-CD; Figs. 3, 4:4-6). Furthermore,

413 after pPEip, but not aPEip injection, robust labelling was found in F2 (Figs. 3, 4:1-5). After the  
414 pPEip injection, the proportion of RLC in F2 (13,4%) was similar to that observed after that in  
415 aMIP (10,9%). However, RLC were almost completely located lateral to the pre-CD, whereas  
416 after the MIP injection they extended also more dorsally (Fig. 3). In both cases, moderate  
417 labelling also involved the ventral premotor area F4 (Figs. 3, 4:3, 5:3-4) and weaker labelling  
418 was observed in F3 (Figs. 3, 4:1-3, 5:4-5). Moderate labelling was observed in areas 24c/d  
419 and 23c (Figs. 3, 4:1-7, 5:1-8).

#### 420 *Projections from parietal cortex*

421 In the SPL, robust labelling to both aPEip and pPEip was observed in area PE, richer after the  
422 aPEip injections (18,3% vs. 11,1%). In this area, RLC very densely packed in the rostral part,  
423 however after the pPEip injection they also extended in the caudal part, which was the PE  
424 sector densely labelled after the MIP injections (Figs. 3, 4:7-12, 5:11-15). Caudal to PE, after  
425 the pPEip injections, labelling was relatively moderate in PEc (4,2%) and PEci (5,3%), weak in  
426 PGM (1,6%), and robust in V6A (10,5%; Figs. 3, 4:13-17). In all these areas, labelling was  
427 much weaker, or even absent after the aPEip injection (Figs. 3, 5:14-19). Similarly, the  
428 number of RLC observed in MIP was much higher after the pPEip (12,9%) than the aPEip  
429 (5,1%) injection.

430 In the IPL, both aPEip and pPEip were moderately connected with the hand-related area  
431 PFG, though after the pPEip injection the labelling moderately involved also PG (Figs. 3, 4:7-  
432 13, 5:5-7). Furthermore, aPEip was characterized by a robust input from PGop (11,7%;  
433 Fig.4:8-10), which was much weaker for pPEip (4,2%), as well as by relatively robust input  
434 from the hand-related area AIP (6,3%) and in VIP (5,5%), where RLC were relatively sparse  
435 after the pPEip injections (Figs. 3, 4:8-12, 5:8-14).

436 After the aPEip injection there was robust labelling in SI (7,3%; Figs. 3, 5: 6-7) and a relatively  
437 weak labelling in SII and the insular cortex, all virtually devoid of labelling after the pPEip  
438 injection. Finally, a weak input from MST was observed in both cases.

439

#### 440 ***Connectivity profiles of aPEip, pPEip, aMIP, and pMIP***

441 To offer a quantitative view of the results, the data reported in Figs. 4-5 and in Table 1 were  
442 expressed in the form of frequency distribution. Figure 6 reports the proportion of RLC (Y

443 axis) across cortical areas, which are arranged from left to right (X axis) according to their  
444 approximate A-P location in the cortex.

445 The frontal input to parietal areas injected in this study stems mostly from areas F2 and M1.  
446 Projections from F2 are mainly addressed to pPEip, aMIP and pMIP, in decreasing order of  
447 magnitude. Motor cortex projections follow a similar pattern but differ for a strong input to  
448 aPEip as well. Area S1 projects only to aPEip. Smaller projections stem from cingulate areas  
449 24c and 23 and from ventral premotor area F4.

450 The parietal projections to PEip and MIP are by far stronger than the frontal ones and  
451 originate mainly from superior parietal areas, such as PE, PEc, from local connections within  
452 PEip and MIP and from V6A, PEci, and PGm. Inferior parietal projections are by far weaker,  
453 and originate from PGop, especially after the injection in aPEip, with smaller contribution  
454 from areas PG and PFG. Finally, aPEip showed a relatively robust connection with areas AIP  
455 and VIP.

456 In several instances, the projections addressed to areas PEip and MIP from cingulate, frontal  
457 and parietal areas followed a gradient-like pattern, as also shown in Fig. 7. Examples are the  
458 projections from area 24c, M1, and PFG, which all project with decreasing strength to aPEip,  
459 pPEip, aMIP and pMIP. The F2 projections to dorsal intraparietal areas display a similar  
460 pattern, if one excludes the scant projection to aPEip. On the contrary, the strength of PEci  
461 projections shows an inverse gradient. The strength of the projections from PE and V6A  
462 waxes and wanes in the A-P extent.

463 A pictorial representation of the gradient-like organization of this part of the parieto-frontal  
464 system can be seen in the brain figurine of Figure 7.

465 ***Segregation and overlap and laminar distribution of frontal and parietal cells projecting to***  
466 ***PEip and MIP***

467 In the tangential domain of the cortex there exists an orderly arrangement of properties that  
468 can relate to the representation of sensory receptors, motor output, visual attention, motor  
469 intention, working memory, etc. Moreover, there is evidence that cortical connections  
470 shape, at least in part, the functional properties of neurons in the parieto-frontal system  
471 (Johnson et al., 1996; Chafee and Goldman-Rakic, 1998, 2000; Battaglia-Mayer et al., 2001).

472 To study whether PEip and MIP share cortical afferents, therefore functional properties, we  
473 compared the tangential distribution of frontal and parietal cells projecting to their anterior



474 and posterior sectors, a study made possible by the injections of two different fluorescent  
475 tracers in each of the two animals.

476 In case 72, where DY was injected in pPEip and FB in aMIP, frontal cells projecting mostly to  
477 pPEip (Fig. 4, see yellow labelling) involve both dorsal premotor area F2 and M1 while those  
478 projecting to aMIP (Fig. 4, see blue labelling) occupy restricted efferent frontal zones, mainly  
479 located in F2. With the exclusion of a restricted part of the latter (Fig. 4:2-3), cell projecting  
480 to pPEip and aMIP were largely segregated in the tangential domain of the cortex. At some  
481 locations, parietal cells projecting to both pPEip and aMIP were segregated (Fig.4:7-17), even  
482 in the same area, as for PGm (Fig.2:14). On the contrary, extensive overlap was found in  
483 areas PEc, PEci and V6A (Fig. 4:14-17).

484 The distribution of cells projecting to aPEip and pMIP, where FB and DY were respectively  
485 injected (Fig. 5) obeys to a similar pattern, where segregation dominates over overlap in  
486 both frontal and parietal projections, although some overlap was observed in areas PGop  
487 (Fig.5:10-11), pPEip (Fig. 5:13-15), aMIP(Fig. 5:15), V6a (Fig. 5:17).

488 When comparing the distribution of cells in the rostral bank of the CS, i.e., in the “new M1”  
489 (Rathelot and Strick, 2009), in both cases 72 and 73 we mostly observed absence of overlap  
490 of cells projecting to the intraparietal areas injected, as well as in area PE and in large part of  
491 aPEip, while a small overlap was confined only to very limited zones of the bank (Fig. 5:6-7).

492 Finally, the analysis of the laminar distribution of RLC in the various frontal and parietal areas  
493 more densely labeled after the injections in different sectors of PEip and MIP showed a  
494 proportion of RLC in the superficial vs. deep layers virtually everywhere within 33% and 66%,  
495 that is a marked bilaminar distribution.

496

#### 497 **DW-MRI study of the db-IPS**

#### 498 *Comparison between the distribution of retrogradely labelled cells and the diffusion-based* 499 *connectivity estimates*

500 We compared the connectivity of the 48 cortical regions obtained through histological  
501 procedures with the intra-axonal MRI signal fraction estimated from DW-MRI. This was  
502 achieved by computing the Pearson’s correlation coefficient between the distribution of RLC  
503 obtained for the four injection sites and the distribution of diffusion-based connectivity  
504 estimated at different locations along the entire extent of the db-IPS (see Material and  
505 Methods). To cover in a continuous fashion the whole IPS, we used a sliding window of 2.5

506 mm, corresponding to five MRI coronal slices, moving in the A-P direction and selecting all  
507 streamlines connecting the MRI slices to the 48 cortical ROIs included in our analysis (see  
508 Material and Methods). To better reproduce the extent of the injection sites of retrograde  
509 tracers in the dorso-ventral dimension, the MRI slices encompassed only the dorsal and  
510 middle sectors of our three-fold subdivision of the db-IPS (Fig. 8B). This choice was dictated  
511 by the histological verification that the tracer injections did not involve the deepest part of  
512 the dorsal bank, as well as by the fact that the latter can hardly be parcellated into three  
513 dorso-ventral section in its most anterior part, given the limited extent of the cortex in this  
514 dimension.

515 In Figure 8A data points in each curve show the Pearson's coefficients for the correlation  
516 between the distribution of RLC obtained for each of the injection sites (aPEip, pPEip, aMIP,  
517 pMIP) and the diffusion-based connectivity of each 2.5mm sliding window along the A-P  
518 dimension of the db-IPS. The X-axis shows the MRI coronal slice number at the center of  
519 each window. The locations with the highest correlation are indicated by the star markers.  
520 The MRI coronal slice number corresponding to each injection site's highest correlation  
521 coefficient (Fig. 8A; star markers) well agrees with the relative position of the injection sites  
522 of neural tracer (Fig. 1). Despite known limitations of DW-MRI connectivity analysis, such as  
523 the presence of false-positive connections, Figure 8A shows that tractography can indeed  
524 identify changes in the connectivity distribution in the A-P dimension of the db-IPS that are  
525 correlated with changes observed using RLC analysis. In fact, the RLC distribution after  
526 injection in aPEip had the highest correlation value ( $r=0.72$ ;  $n=34$ ;  $p=1.1 \cdot 10^{-8}$ ) at slice 99,  
527 after injection in pPEip at slice 95 ( $r=0.41$ ;  $n=48$ ;  $p=0.004$ ), showing however similar  
528 correlation values (plateau) at different A-P locations ranging from slice 97 to 89, while after  
529 injection in aMIP the correlation peaked at slice 88 ( $r=0.81$ ;  $n=34$ ;  $p=1.9 \cdot 10^{-12}$ ) and after  
530 injection in pMIP at slice 78 ( $r=0.66$ ;  $n=34$ ;  $p=3.9 \cdot 10^{-7}$ ). This highlights the sensitivity of the  
531 DW-MRI connectivity to the changes measured by the RLC analysis in the fine parcellation of  
532 the db-IPS.

533 When selecting the locations with highest correlation for each of the four injection sites, the  
534 overall correlation between the diffusion-based connectivity estimation and the RLC  
535 distribution was  $r=0.65$  ( $n=192$ ,  $p=1.7 \cdot 10^{-24}$ ).

536 The changes of the correlation coefficient between the distributions of labelled cells and  
537 diffusion connectivity across the db-IPS are shown in Figure 8B, by using a diffusion MRI  
538 derived anatomical rendering of the overall the bank and facilitate the comprehension on

539 the areas involved in this analysis. It can be seen that the highest correlation was found in a  
540 region spanning the central part (in A-P dimension) and dorso/middle sectors (in D-V  
541 dimension) of the bank, after injections in aMIP. A good correlation was also found in the  
542 anterior third of the bank after injections in aPEip, while the correlation decreased, although  
543 to a different extent, after injections in pPEip and pMIP. The implication of these results for  
544 the gradients in the connectivity profiles of the dorsal intraparietal areas will be dealt with in  
545 the Discussion. The corresponding distribution of RLC for the four injection sites alongside  
546 the diffusion-based connectivity for the locations with the maximum Pearson's coefficients  
547 are reported in Figure 9, together with the relative MRI slices and drawing of the histological  
548 sections.

549 For the four injections sites there are 192 (48 areas x 4 injections) potential ROIs  
550 connections, among which 113 have non-zero labelled cell counts. Diffusion tractography  
551 shows an average of 90.4% of the connection's weights for ROIs with non-zero reported  
552 labelled cells. Moreover, tractography correctly identified 107 connections (true-positive  
553 connections; TP), thus missing only 5 connections (false-negative connection; FN).  
554 Tractography correctly reported no connectivity for 44 ROIs (true negative connections; TN),  
555 but estimated connectivity for 36 ROIs where no labelled cells were found (false positive  
556 connections; FP).

557 The overall data analysis resulted in a sensitivity of  $0.96 \left( \frac{TP}{TP+FN} \right)$  and a specificity of 0.55  
558  $\left( \frac{TN}{TN+FP} \right)$ .

559 Across the matching locations and all cortical ROIs, the connection with the most  
560 underestimated fraction of diffusion-based connectivity (-0.143) is ROI F2, after injection site  
561 in aMIP. This is followed by connection F1-aMIP (-0.135), F1-pMIP (-0.126), F2-aPEip (-0.111)  
562 and F2-pPEip (-0.109). Similarly, the most overestimated connectivity is PGm-aPEip (+0.173),  
563 followed by PE-aMIP (+0.151), PE-pMIP (+0.109), S1-aMIP (+0.103) and VIP-aMIP (+0.096).  
564 Across the four matching site's location, tractography misestimated the connectivity the  
565 most on ROIs F2, PE, M1, VIP and LIP. As examples, contrary to tracer data, our tractography  
566 estimations showed streamlines connecting both sectors of PEip (Fig. 9A-B) and MIP (Fig. 9C-  
567 D) to LIP. However, previous histological studies had shown connections between LIP and  
568 MIP (Bakola et al., 2017) and LIP and PEip (referred to as PEa; Blatt et al., 1990).  
569 Furthermore, our study shows connections between aPEip and S1 (Fig. 9A) which are  
570 stronger from tractography than histology. It also reveals streamlines between S1 and pPEip

571 (Fig.9B) and both sectors of MIP (Fig. 9C-D) which are not matched by histology (see also  
572 Table 1). Finally, cell counts show strong connectivity between F2 and pPEip (Fig.9B), as well  
573 as with and both sectors of MIP (fig. 9C-D), which is not matched by tractography.

574

#### 575 ***Diffusion-based connectivity profiles along the db-IPS***

576 As a next step, we evaluated in a quantitative fashion the degree of similarity of the  
577 diffusion-based connectivity estimation along the db-IPS. To this aim, we computed the  
578 Pearson's correlation coefficient between all sliding windows. Figure 10A shows the  
579 Pearson's correlation coefficient between the distributions of diffusion-based connectivity  
580 estimated in different sliding windows along the A-P extent of the db-IPS. The X and Y axes  
581 show the MRI coronal slice number corresponding to the center of each window. A strong  
582 correlation is expected between locations distant four or less MRI slices apart, due to the  
583 windows overlap. A decrease in correlation can be observed when the distance between  
584 windows increases in the A-P extent of the bank. This suggests a general gradient-like  
585 organization, where the pattern of cortical connectivity gradually changes. Visual inspection  
586 of the correlation matrix highlights the existence of three potential clusters, located  
587 anteriorly, centrally and posteriorly along the bank, that can be identified by their highest  
588 correlations (range 1- 0.6) between neighboring locations. This suggests that along the A-P  
589 extent of the db-IPS there might exist three broad connectionally different regions. A similar  
590 matrix (Fig. 10B) is shown for selected locations corresponding to the four MRI windows with  
591 the highest correlation between the diffusion-based and tract tracing connectivity (see also  
592 Fig. 8). It can be seen that similar results were obtained when correlating the pattern of  
593 connectivity obtained from histological tracing data, after injections in intraparietal areas  
594 aPEip, pPEip, aMIP, and pMIP.

595

#### 596 ***DW-MRI connectivity estimates of the dorsal, middle and ventral sectors of the db-IPS***

597 Furthermore, we investigated the cortical connectivity of the dorsal, middle and ventral  
598 sectors of the db-IPS using diffusion MRI. It is worth stressing, the cortical regions lying in the  
599 more ventral and deep part of the bank can be hardly accessed by neural tracer injections,  
600 therefore their connectivity remains virtually unknown. The sum of the diffusion-based  
601 connectivity calculated across the 38 different A-P locations (MRI slices) for the dorsal,  
602 middle and ventral sectors is shown in Figure 11. The parietal areas VIP, V6A, PE, LIP, PEc,

603 PGm, and SI are the ROIs showing the overall strongest connectivity with the bank, among  
604 the 48 ROIs considered in this study. However, clear differences emerge in the streamline  
605 contribution provided by specific portions of the IPS along the dorso-ventral dimension.

606

607 To highlight this aspect, we report the results (Fig. 12) referring to the connectivity occurring  
608 between each of the 12 most connected cortical areas (i.e., VIP, V6A, PE, LIP, PEc, PGm, SI,  
609 PEci, AIP, PFG, PG, M1; see Fig. 11), and the A-P and D-V extent of the db-IPS. Each image  
610 shows the spatial distribution of the diffusion-based connectivity, along the 38 A-P dorsal,  
611 middle and ventral subdivisions of the bank, for each of the 12 cortical ROIs listed above. The  
612 sectors displaying strong connectivity with the indicated cortical ROI are shown in yellow and  
613 orange. It can be seen that there exists a smooth transition in the strength of connectivity in  
614 both the A-P and D-V dimensions of the bank. The IPS region more strongly connected with  
615 area VIP is the most anterior sector of the bank, with a gradual reduction moving posteriorly,  
616 while for V6A is the postero-ventral part of the bank, as also observed from tract tracing  
617 data on the proportion of RLC (see Fig. 7). Area PE instead display a more diffuse pattern of  
618 connectivity along the D-V dimension of the anterior part of the bank. LIP connectivity  
619 occurs exclusively with the regions located in the more ventral part of the dorsal bank, close  
620 to the fundus of the IPS. Another example of a gradient-like distribution of connectivity,  
621 along both the A-P and D-V dimensions is offered by PEc, whose connectivity is strongest  
622 with the dorsal and intermediate part of the bank. The connectivity of PGm resembles that  
623 of V6A, but it is weaker and more diffuse in the A-P extent of the ventral part of the  
624 intermediate sectors. Area SI is strongly connected with the D-V extent of the rostralmost  
625 part of the bank, while the connections of PEci are more selective, since they occur mainly  
626 with the central part of the bank, are stronger dorsally and fade away moving ventrally,  
627 anteriorly and posteriorly. The inferior parietal areas AIP, PFG, and PG show a weak  
628 connectivity with the anterior part of the ventral sector of the bank, while motor cortex (M1)  
629 is weakly connected with its antero-dorsal sector.

630

## 631 **DISCUSSION**

632 The results of this study provide solid support for a parcellation of the db-IPS into a rostral  
633 area PEip and a caudal area MIP, based on corticospinal projections, as well as for an internal  
634 subdivision of both areas into an anterior and posterior sector. Our data also show antero-

635 posterior and dorso-ventral connectional gradients, matching those of functional properties  
636 described by electrophysiological studies. In the A-P extent of the SPL Crammond and  
637 Kalaska (1989) and Burbaud et al. (1991) showed that activity in area PE is mostly related to  
638 somatosensory function, while Colby and Duhamel (1991) in MIP described a set visuomotor  
639 functions. A combined anatomo-functional analysis of the parieto-frontal system (Johnson et  
640 al., 1996) in monkeys revealed that reaching-related neurons displaying signal-, set-,  
641 movement- and positional-related activity decreased in numbers moving from ventral to  
642 dorsal in MIP, up to PE. Furthermore, parietal and frontal regions displaying similar activity  
643 types were linked by direct cortico-cortical connections.

#### 644 **Cortical connections of the db-IPS**

645 Our data are in line but also extend data from Bakola et al. (2017), where MIP defined  
646 myeloarchitectonically extends rostrally up to the A-P level of the caudal end of the central  
647 sulcus, thus including the caudalmost part of the corticospinal sector of the db-IPS.  
648 Our tracer injections in MIP show a relatively strong connectivity with visuomotor areas V6A,  
649 PEc, PEip, and F2. Weaker connections involve the IPL visuomotor area PG, area PGop and  
650 M1. Furthermore, aMIP, when compared to pMIP, shows stronger connectivity with area PE  
651 and visuomotor area PGm, a weaker one with somatosensory area PEci. This connectivity  
652 pattern of MIP conforms to that reported by Bakola et al (2017) for the caudal part of this  
653 area. Furthermore, indirect support for this connectivity scheme and for the reciprocity  
654 characterizing MIP connections comes from studies in which this area was labelled after  
655 retrograde tracer injections in V6A (Marconi et al., 2001; Gamberini et al., 2009; Passarelli et  
656 al., 2011), PEc and PE (Marconi et al., 2001; Bakola et al., 2010; 2013), PGm (Passarelli et al.,  
657 2018), PG (Rozzi et al., 2006) and F2 (e.g., Johnson et al., 1996; Matelli et al., 1998; Marconi  
658 et al., 2001; Tanné et al., 2002). Thus, the connectivity of MIP provides a neural substrate for  
659 the visuomotor control of reaching and eye-hand coordination, since it can serve as interface  
660 between the premotor areas of the frontal lobe and the parieto-occipital areas V6A and PEc,  
661 where neurons combine in a directionally- congruent fashion eye- and hand-related  
662 positional- and movement-related signals within their directional tuning fields (Battaglia-  
663 Mayer et al., 2000, 2001). Interestingly, similar inputs to MIP come from PGm (7m), where  
664 individual neurons also combine visual, eye and hand related signals (Ferraina et al., 1997a,  
665 b).

666 A model relevant to eye-hand coordination (Mascaro et al., 1983) integrating inputs from  
667 the retinal position of the target with eye- and hand position shows that both feedforward  
668 and recurrent interactions of these signals account very well for the experimentally observed  
669 tuning fields of parietal neurons. In this model, the representation of directional variables  
670 concerning hand and eye movement emerges from Hebbian synaptic plasticity alone (see  
671 Battaglia-Mayer and Caminiti 2002; Battaglia-Mayer et al., 2015; Battaglia-Mayer and  
672 Caminiti, 2017).

673 Our data also show that area PEip is a db-IPS sector displaying as unifying connectional  
674 features robust connectivity with the cervical spinal cord and the hand field of M1. Strong  
675 connections with area PE and with visuomotor hand-related area PFG (Ferrari-Toniolo et al.,  
676 2015), bimodal visual and somatosensory area VIP, and area F4 further characterize PEip.  
677 The caudal part of PEip also displays connections with V6A and F2 and a connectivity pattern  
678 with areas PEci, PEc, and PG quantitatively more similar to that of aMIP. In contrast, aPEip  
679 displays connections with the arm/hand field of SI, the hand-related area AIP and a strong  
680 connectivity with PGop, whose function remain unknown. The connectivity observed after  
681 tracer injections in pPEip and aPEip is very similar to that observed by Bakola et al. (2017)  
682 after an injection in rostral myeloarchitectonic area MIP and in area PEip, respectively.  
683 Connections with PEip have been observed after retrograde tracer injections in areas V6A  
684 (Gamberini et al., 2009), PE (Bakola et al., 2013), PFG (Rozzi et al., 2006), AIP (Borra et al.,  
685 2008; Lanzilotto et al, 2019), F2 (e.g., Johnson et al., 1996; Matelli et al., 1998; Tanné et al.,  
686 2002) and M1 (Strick and Kim, 1978; Matelli et al., 1986; Hatanaka et al., 2001). This  
687 connectivity suggests a role of PEip in sensorimotor control of hand movements. Indeed,  
688 PEip as a whole coincides with the db-IPS sector hosting corticospinal neurons projecting to  
689 distal hand muscles motoneurons (Rathelot et al. 2017), as well as neurons with  
690 somatosensory receptive fields on the hand (Iwamura et al., 1994; Iwamura 2000; Seelke et  
691 al., 2012). The posterior part of PEip could also correspond to the sector hosting neurons  
692 with bimodal, visual and somatosensory receptive field centred on the hand (Iriki et al.,  
693 1996) and the anterior PEip to the sector rich in grasping-related neurons (Gardner et al.  
694 2007). The connectional differences between the posterior and the anterior part of PEip,  
695 suggest for the former a role in visuo- and somato-motor control of hand and arm  
696 movements, and for the latter a role in somato-motor control of hand actions.

697 **Diffusion-based connectivity estimations**

698 We have used state-of-the-art tractography algorithm and microstructure method to  
699 estimate the intra-axonal MRI signal fraction associated with streamlines, instead of using  
700 their number. This reduced density biases associated with white matter bundle features,  
701 such as length, curvature, and size, making tractography more quantitative (Daducci, et al.  
702 2014; Girard et al., 2014). This goal was achieved by using a model of tissue microstructure  
703 (Stick-Zeppelin-Ball model, Panagiotaki et al., 2012, Daducci et al., 2014) to explain the  
704 measured DW-MRI signal from the streamlines, by removing or penalizing redundant or  
705 inaccurate trajectories. In a previous study, Girard et al. (2020) compared various diffusion-  
706 based connectivity estimation approaches in the monkey brain and showed that this model  
707 had strong performances in the prediction of parieto-frontal binary connectivity (sensitivity  
708 and specificity). Moreover, it had the highest fraction of valid connectivity weight among  
709 methods with high sensitivity and specificity.

710

711 In the connectivity network emerging after the four injections made within the db-IPS, our  
712 results showed an increased sensitivity of 0.96 (from 0.79) and a decreased specificity of  
713 0.55 (from 0.60), as compared to the analysis of the parieto-frontal network we made before  
714 (Girard et al., 2020). Overall, this resulted in an increased Youden's index (Sensitivity +  
715 Specificity – 1; Youden, 1950) to 0.51 vs. the 0.39 reported in Girard et al. (2020). Moreover,  
716 in the network studied here, we found 90.4% of the connectivity weights between ROIs with  
717 reported non-zero labelled cell count, 10.2% more than in Girard et al. (2020). This suggests  
718 a strong predictive power of tractography for the connectivity of the monkeys IPS, which  
719 was also confirmed by the lack of connections with prefrontal areas shown by both  
720 histological and tractography results.

721

722 In addition to the rostro-caudal gradients evidenced by the tracer injections, the  
723 tractography estimated connectivity showed along the db-IPS clear dorso-ventral gradients  
724 which would have been difficult to demonstrate based on tracer injections. These consisted  
725 in a preferential connectivity of ventral sectors of the bank with visuomotor areas V6A, PGM,  
726 and LIP and a preferential connectivity of middle and dorsal sectors with SI, PE, PEci, PEC,  
727 thus matching the increase in visually responsive neurons moving from the dorsal to the  
728 ventral in the bank (Colby and Duhamel 1991; Johnson et al., 1996; see Battaglia- Mayer et  
729 al., 2016). Dorsoventral chemoarchitectonic differences within the db-IPS, waiting for



730 functional and/or connectional correlation, have been observed based on receptor  
731 autoradiography (Niu et al 2020).

732

733 Our overall correlation coefficient of the diffusion-based connectivity and of the RLC  
734 distribution ( $r=0.65$ ) goes in line with the results ( $r=0.59$ ) reported by Donahue et al. (2016).

735 These authors studied the predictive power of tractography for connection weights derived  
736 from 29 retrograde tracer injections and 91 brain areas, reported by Markov et al. (2014).

737 Although we have used different tractography algorithms and connectivity weights  
738 estimation from DW-MRI, both Donahue et al. (2016) and our study show that tractography  
739 can indeed estimate structural connectivity weights correlated with the number of  
740 measured labelled cells connecting cortical areas.

#### 741 **Tractography misestimated connections**

742 Although tractography produces weighted connectivity proportions showing a good  
743 correlation with the proportions of labelled cells, and that most of the weights are in  
744 connections with non-zero measured labelled cell count, some connection weights were  
745 misestimated.

746 The source of these misestimations can be related, in part, to the uni-directional labelling of  
747 cells from retrograde axonal tracing used in this study. Thus, asymmetry in the afferent and  
748 efferent axon densities of a fascicle could result in a mismatch between the two techniques.  
749 The diffusion-based connectivity was estimated from ROIs in the db-IPS that were larger  
750 than the injection site of tracers, thus reporting the connectivity of a broader sector.  
751 Moreover, the intricate white matter geometries and configurations, such as crossing and  
752 kissing, could have resulted in incorrect orientations and erroneous trajectories (see  
753 Jeurissen et al. 2017 and Girard et al., 2020). Finally, the accuracy of diffusion-based  
754 connectivity is limited by the model of the white matter used, which can fail to accurately  
755 model the diffusion signal in intricate microstructure environments (Jelescu et al., 2020).  
756 Future work should target analysis of ROIs with misestimated connectivity, using DW-MRI  
757 and bi-directional tracing data of the same animal.

758

759

760

761

762

763 **REFERENCES**

764

765 Ahmed B, Cordery PM, McLelland D, Bair W, Krug K (2012) Long-range clustered connections  
766 within extrastriate visual area V5/MT of the rhesus macaque. *Cereb Cortex* 22:60–73.

767 Ambrosen KS, Eskildsen SF, Hinne M, Krug K, Lundell H, Schmidt MN, van Gerven MAJ,  
768 Mørup M, Dyrby TB. Validation of structural brain connectivity networks: The impact of  
769 scanning parameters (2020) Validation of structural brain connectivity networks: The  
770 impact of scanning parameters. *NeuroImage* 204:116–207.

771 Aydogan DB, Jacobs R, Dulawa S, Thompson SL, Francois MC, Toga AW, Dong H, Knowles JA,  
772 Shi Y (2018) When tractography meets tracer injections: a systematic study of trends and  
773 variation sources of diffusion-based connectivity. *Brain Struct Funct* 223:2841–2858.

774 Azadbakht H, Parkes LM, Haroon HA, Augath M, Logothetis NK, de Crespigny A, D'Arceuil HE,  
775 Parker GJ (2015) Validation of high-resolution tractography against in vivo tracing in the  
776 macaque visual cortex. *Cereb Cortex* 25:4299–4309.

777 Bakola S, Gamberini M, Passarelli L, Fattori P, Galletti C (2010) Cortical connections of  
778 parietal field PEc in the macaque: linking vision and somatic sensation for the control of  
779 limb action. *Cereb Cortex* 20:2592–604.

780 Bakola S, Passarelli L, Gamberini M, Fattori P, Galletti C (2013) Cortical connectivity suggests  
781 a role in limb coordination for macaque area PE of the superior parietal cortex. *J Neurosci*  
782 33:6648–58.

783 Bakola S, Passarelli L, Huynh T, Impieri D, Worthy KH, Fattori P, Galletti C, Burman KJ, Rosa  
784 MGP (2017) Cortical Afferents and Myeloarchitecture Distinguish the Medial Intraparietal  
785 Area (MIP) from Neighboring Subdivisions of the Macaque Cortex. *eNeuro*, 4(6),  
786 ENEURO.0344-17.2017.

787 Balint R (1909) Seelenlähmung des "Schauens", optische ataxia, räumliche störung der  
788 aufmerksamkeit. *M Schr Psychiat Neurol* 25:51–66.

789 Batista AP, Buneo CA, Snyder LH, Andersen RA (1999) Reach plans in eye-centered  
790 coordinates. *Science* 285: 257-260.

791 Battaglia-Mayer A, Ferraina S, Mitsuda T, Marconi B, Genovesio A, Onorati P, Lacquaniti F,  
792 Caminiti R (2000) Early coding of reaching in the parieto-occipital cortex. *J Neurophysiol*  
793 83:2374-2391.

794 Battaglia-Mayer A, Ferraina S, Genovesio A, Marconi B, Squatrito S, Molinari M, Lacquaniti F,  
795 Caminiti R (2001) Eye-hand coordination during reaching. II. An analysis of the  
796 relationships between visuomanual signals in parietal cortex and parieto-frontal  
797 association projections. *Cereb Cortex* 11:528–544.

- 798 Battaglia-Mayer A, Caminiti R (2002) Optic ataxia as a result of the breakdown of the global  
799 tuning fields of parietal neurones. *Brain* 125:25–237.
- 800 Battaglia-Mayer A, Ferrari-Toniolo S, Visco-Comandini F (2015) Timing and communication of  
801 parietal cortex for visuomotor control. *Curr Opin Neurobiol* 33:103–109.
- 802 Battaglia-Mayer A, Babicola L, Satta E (2016) Parieto-frontal gradients and domains  
803 underlying eye and hand operations in the action space. *Neuroscience* 334:76–92.
- 804 Battaglia-Mayer A, Caminiti R (2018) Parieto-frontal networks for eye-hand coordination and  
805 movements. *Handb Clin Neurol* 151:499–524.
- 806 Battaglia-Mayer A, Caminiti R (2019a) Corticocortical Systems Underlying High-Order Motor  
807 Control. *J Neurosci* 23:4404–4421.
- 808 Belmalih A, Borra E, Contini M, Gerbella M, Rozzi S, Luppino G. (2009) Multimodal  
809 architectonic subdivision of the rostral part (area F5) of the macaque ventral premotor  
810 cortex. *J Comp Neurol.* 512:183–217
- 811 Blatt GJ, Andersen RA, Stoner GR (1990) Visual receptive field organization and cortico-  
812 cortical connections of the lateral intraparietal area (area LIP) in the macaque. *J Comp*  
813 *Neurol* 299:421–445.
- 814 Borra E, Belmalih A, Calzavara R, Gerbella M, Murata A, Rozzi S, Luppino G (2008) Cortical  
815 connections of the macaque anterior intraparietal (AIP) area. *Cerebral cortex* 18:1094–  
816 1111.
- 817 Borra E, Belmalih A, Gerbella M, Rozzi S, Luppino G (2010) Projections of the hand field of  
818 the macaque ventral premotor area F5 to the brainstem and spinal cord. *J Comp Neurol*  
819 518: 2570–2591.
- 820 Burbaud P, Doegle C, Gross C, Bioulac B (1991) A quantitative study of neuronal discharge in  
821 areas 5, 2, and 4 of the monkey during fast arm movements. *J Neurophysiol* 66:429–443.
- 822 Calabrese E, Badea A, Cofer G, Qi Y, Johnson G A (2015) A Diffusion MRI tractography  
823 connectome of the mouse brain and comparison with neuronal tracer data. *Cereb*  
824 *Cortex* 25:4628–4637.
- 825 Caminiti R, Johnson PB, Galli C, Ferraina S, Burnod Y (1991) Making arm movements within  
826 different parts of space: the premotor and motor cortical representation of a coordinate  
827 system for reaching to visual targets. *J Neurosci* 11:1182–1197.
- 828 Caminiti R, Ferraina S, Johnson PB (1996) The sources of visual information to the primate  
829 frontal lobe: a novel role for the superior parietal lobule. *Cereb Cortex* 6:319–328.

- 830 Caminiti R, Borra E, Visco-Comandini F, Battaglia-Mayer A, Averbeck BB, Luppino G (2017)  
831 Computational architecture of the parieto-frontal network underlying cognitive-motor  
832 control in monkeys. *eNeuro* 4(1), ENEURO.0306–16.2017.
- 833 Carmichael ST, Price JL. (1994) Architectonic subdivision of the orbital and medial prefrontal  
834 cortex in the macaque monkey. *J Comp Neurol.* 346:366–402.
- 835 Chafee MV, Goldman-Rakic PS (1998) Matching patterns of activity in primate prefrontal  
836 area 8a and parietal area 7ip neurons during a spatial working memory task. *J*  
837 *Neurophysiol* 79:2919–40.
- 838 Chafee MV, Goldman-Rakic PS (2000) Inactivation of parietal and prefrontal cortex reveals  
839 interdependence of neural activity during memory-guided saccades. *J Neurophysiol*  
840 83:1550–1566.
- 841 Colby CL, Gattass R, Olson CR, Gross CG. (1988) Topographical organization of cortical  
842 afferents to extrastriate visual area PO in the macaque: a dual tracer study. *J Comp*  
843 *Neurol.* 269:392-413.
- 844 Colby CL, Duhamel JR (1991) Heterogeneity of extrastriate visual areas and multiple parietal  
845 areas in the macaque monkey. *Neuropsychologia* 29:517–37.
- 846 Condé F (1987) Further studies on the use of the fluorescent tracers fast blue and diamidino  
847 yellow: effective uptake area and cellular storage sites. *J Neurosci Methods* 21:31–43.
- 848 Crammond DJ, Kalaska JF (1989) Neuronal activity in primate parietal cortex area 5 varies  
849 with intended movement direction during an instructed-delay period. *Exp Brain Res*  
850 76:458–62.
- 851 Daducci A, Dal Palu A, Lemkaddem A, Thiran JP (2014) COMMIT: Convex Optimization  
852 Modeling for Micro-structure Informed Tractography. *IEEE Trans Med Imaging*, 34:246–  
853 257.
- 854 Dauguet J, Peled S, Berezovskii V, Delzescaux T, Warfield SK, Born R, Westin CF (2007)  
855 Comparison of fiber tracts derived from in-vivo DTI tractography with 3D histological  
856 neural tract tracer reconstruction on a macaque brain. *NeuroImage* 37:530–538.
- 857 Delettre C et al. (2019) Comparison between diffusion MRI tractography and histological  
858 tract-tracing of cortico-cortical structural connectivity in the ferret brain. *Netw Neurosci*  
859 3:1038-1050.
- 860 Demelio S, Bettio F, Gobetti E, Luppino G (2001) Three-dimensional reconstruction and  
861 visualization of the cerebral cortex in primates. In: Ebert D, Favre J, Peikert R, editors.  
862 *Data Visualization 2001. Proceedings of the Joint Eurographics and IEEE TCVG Symposium*  
863 *on Visualization, Ascona, Switzerland, May 28–30, 2001.*

- 864 Donahue CJ et al. (2016) Using Diffusion Tractography to Predict Cortical Connection  
865 Strength and Distance: A Quantitative Comparison with Tracers in the Monkey. *J Neurosci*  
866 36:6758-70.
- 867 Dyrby TB, Sjøgaard LV, Parker GJ, Alexander DC, Lind NM, Baaré WF, Hay-Schmidt A, Eriksen  
868 N, Pakkenberg B, Paulson OB (2007) Validation of in vitro probabilistic tractography.  
869 *Neuroimage* 37:1267–1277.
- 870 Dyrby TB, Baaré WF, Alexander DC, Jelsing J, Garde E, Sjøgaard LV (2011) An ex vivo imaging  
871 pipeline for producing high-quality and high-resolution diffusion-weighted imaging  
872 datasets. *Hum Brain Mapp* 32:544–563.
- 873 Ferraina S, Garasto MR, Battaglia-Mayer A, Ferraresi P, Johnson PB, Lacquaniti F, Caminiti R  
874 (1997a) Visual control of hand-reaching movement: activity in parietal area 7m. *Eur J*  
875 *Neurosci* 9:1090–1095.
- 876 Ferraina S, Johnson PB, Garasto MR, Battaglia-Mayer A, Ercolani L, Bianchi L, Lacquaniti F,  
877 Caminiti R (1997b) Combination of hand and gaze signals during reaching: activity in  
878 parietal area 7m of the monkey. *J Neurophysiol* 77:1034–1038.
- 879 Ferrari-Toniolo S, Visco-Comandini F, Papazachariadis O, Caminiti R, Battaglia-Mayer A  
880 (2015) Posterior parietal cortex encoding of dynamic hand force underlying hand-object  
881 interaction. *J Neurosci* 35: 10899–10910.
- 882 Fogassi L, Raos V, Franchi G, Gallese V, Luppino G, Matelli M (1999) Visual responses in the  
883 dorsal premotor area F2 of the macaque monkey. *Exp Brain Res* 128:194–199.
- 884 Gamberini M, Passarelli L, Fattori P, Zucchelli M, Bakola S, Luppino G, Galletti C (2009)  
885 Cortical connections of the visuomotor parietooccipital area V6Ad of the macaque  
886 monkey. *J Comp Neurol* 513:622–42.
- 887 Gardner EP, Babu KS, Reitzen SD, Ghosh S, Brown AS, Chen J, Hall AL, Herzlinger MD,  
888 Kohlenstein JB, Ro JY (2007) Neurophysiology of prehension. I. Posterior parietal cortex  
889 and object-oriented hand behaviors. *J Neurophysiol* 97:387–406.
- 890 Garyfallidis E, Brett M, Amirbekian B, Rokem A, van der Walt S, Descoteaux M, Nimmo-Smith  
891 I (2014) Dipy, a library for the analysis of diffusion MRI data. *Front Neuroinform*, 8:8.
- 892 Gerbella M, Belmalih A, Borra E, Rozzi S, Luppino G. (2007) Multimodal architectonic  
893 subdivision of the caudal ventrolateral prefrontal cortex of the macaque monkey. *Brain*  
894 *Struct Funct.* 212:269–301.
- 895 Girard G, Whittingstall K, Deriche R, Descoteaux M (2014) Towards quantitative connectivity  
896 analysis: reducing tractography biases. *Neuroimage* 98:266–278.

- 897 Girard G, Caminiti R, Battaglia-Mayer A, St-Onge E, Ambrosen KS, Eskildsen SF, Krug K, Dyrby  
898 TB, Descoteaux M, Thiran JP, Innocenti GM (2020) On the cortical connectivity in the  
899 macaque brain: A comparison of diffusion tractography and histological tracing data.  
900 *Neuroimage* 221:117201.
- 901 Gyengesi E, Calabrese E, Sherrier MC, Johnson GA, Paxinos G, Watson C (2014) Semi-  
902 automated 3D segmentation of major tracts in the rat brain: comparing DTI with standard  
903 histological methods. *Brain Struct Funct* 219:539–550.
- 904 Hatanaka N, Nambu A, Yamashita A, Takada M, Tokuno H (2001) Somatotopic arrangement  
905 and corticocortical inputs of the hindlimb region of the primary motor cortex in the  
906 macaque monkey. *Neurosci Res* 40:9–22.
- 907 Iriki A, Tanaka M, Iwamura Y (1996) Coding of modified body schema during tool use by  
908 macaque postcentral neurones. *Neuroreport* 7:2325–30.
- 909 Iwamura Y, Iriki A, Tanaka M (1994) Bilateral hand representation in the postcentral  
910 somatosensory cortex. *Nature* 369:554–6.
- 911 Iwamura Y (2000) Bilateral receptive field neurons and callosal connections in the  
912 somatosensory cortex. *Philos Trans R Soc Lond B Biol Sci* 355:267–73.
- 913 Jbabdi S, Sotiropoulos SN, Haber SN, Van Essen DC, Behrens TE (2015) Measuring  
914 macroscopic brain connections in vivo. *Nat Neurosci* 18:1546–1555.
- 915 Jelescu IO, Palombo M, Bagnato F, Schilling, KG (2020). Challenges for biophysical modeling  
916 of microstructure. In *J Neurosci Methods* (Vol. 344). Elsevier B.V.
- 917 Jeurissen B, Tournier JD, Dhollander T, Connelly A, Sijbers J (2014) Multi-tissue constrained  
918 spherical deconvolution for improved analysis of multi-shell diffusion MRI data.  
919 *NeuroImage* 103:411–426.
- 920 Jeurissen B., Descoteaux M, Mori S, Leemans A (2017) Diffusion MRI fiber tractography of  
921 the brain. *NMR in Biomedicine*, e3785.
- 922 Johnson PB, Ferraina S, Bianchi L, Caminiti R (1996) Cortical networks for visual reaching:  
923 physiological and anatomical organization of frontal and parietal lobe arm regions. *Cereb*  
924 *Cortex* 6:102-119.
- 925 Jones DK, Knösche TR, Turner R (2013) White matter integrity, fiber count, and other  
926 fallacies: The do's and don'ts of diffusion MRI. *Neuroimage* 73:239–254.
- 927 Knösche TR, Anwender A, Liptrot M, Dyrby TB (2015) Validation of tractography: comparison  
928 with manganese tracing. *Hum Brain Map* 36:4116–4134.

- 929 Kuypers HGJM, Huisman AM (1984) Fluorescent Neuronal Tracers. In: *Advances in Cellular*  
930 *Neurobiology*, Vol. 5 (Fedoroff S, ed) pp307-340. New York: Academic Press.
- 931 Lacquaniti F, Guigon E, Bianchi L, Ferraina S, Caminiti R (1995) Representing spatial  
932 information for limb movement: the role of area 5 in the monkey. *Cereb Cortex* 5: 391-  
933 409.
- 934 Lanzilotto M et al. (2019) Anterior Intraparietal Area: A Hub in the Observed Manipulative  
935 Action Network. *Cereb Cortex*. 29:1816–1833.
- 936 Luppino G, Matelli M, Camarda R, Rizzolatti G (1994) Corticospinal projections from mesial  
937 frontal and cingulate areas in the monkey. *Neuroreport* 5:2545–2548.
- 938 Luppino G, Ben Hamed S, Gamberini M, Matelli M, Galletti C (2005) Occipital (V6) and  
939 parietal (V6A) areas in the anterior wall of the parieto-occipital sulcus of the macaque: a  
940 cytoarchitectonic study. *Eur J Neurosci* 21:3056–3076.
- 941 Maier-Hein KH et al. (2017) The challenge of mapping the human connectome based on  
942 diffusion tractography. *Nat Commun* 8:1349.
- 943 Matelli M, Luppino G, Rizzolatti G. (1985) Patterns of cytochrome oxidase activity in the  
944 frontal agranular cortex of the macaque monkey. *Behav Brain Res*. 18:125–136.
- 945 Matelli M, Luppino G, Rizzolatti G. (1991) Architecture of superior and mesial area 6 and the  
946 adjacent cingulate cortex in the macaque monkey. *J Comp Neurol*. 311:445–462.
- 947 Mascaró M, Battaglia-Mayer A, Nasi L, Amit DJ, Caminiti R (2003) The eye and the hand:  
948 Neural mechanisms and network models for oculomanual coordination in parietal  
949 cortex. *Cereb Cortex* 13:1276–1286.
- 950 Marconi B, Genovesio A, Battaglia-Mayer A, Ferraina S, Squatrito S, Molinari M, Lacquaniti F,  
951 Caminiti R (2001) Eye-hand coordination during reaching. I. Anatomical relationships  
952 between parietal and frontal cortex. *Cereb Cortex* 11:513-527.
- 953 Markov NT et al. (2014) A weighted and directed interareal connectivity matrix for macaque  
954 cerebral cortex. *Cereb Cortex* 24:17–36.
- 955 Matelli M, Govoni P, Galletti C, Kutz DF, Luppino G (1998) Superior area 6 afferents from the  
956 superior parietal lobule in the macaque monkey. *J Comp Neurol* 402:327–352.
- 957 Mesulam MM Principles of horseradish peroxidase neurohistochemistry and their  
958 applications for tracing neural pathway. In: *Tracing neural connections with horseradish*  
959 *peroxidase* (Mesulam MM, ed), pp11–52. Chichester (UK): Wiley.



- 960 Niu M, Impieri D, Rapan L, Funck T, Palomero-Gallagher N, Zilles K. Receptor-driven,  
961 multimodal mapping of cortical areas in the macaque monkey intraparietal sulcus. (2020)  
962 *Elife*. Jul 2; 9:e55979. doi: 10.7554/eLife.55979.
- 963 Panagiotaki E, Schneider T, Siow B, Hall MG, Lythgoe MF, Alexander DC (2012) Compartment  
964 models of the diffusion MR signal in brain white matter: a taxonomy and comparison.  
965 *NeuroImage* 59:2241–2254.
- 966 Pandya DN, Seltzer B (1982) Intrinsic connections and architectonics of posterior parietal  
967 cortex in the rhesus monkey. *J Comp Neurol* 204:196–210.
- 968 Passarelli L, Rosa MG, Gamberini M, Bakola S, Burman KJ, Fattori P, Galletti C (2011) Cortical  
969 connections of area V6Av in the macaque: a visual-input node to the eye/hand  
970 coordination system. *J Neurosci* 31:1790–801.
- 971 Passarelli L, Rosa MGP, Bakola S, Gamberini M, Worthy KH, Fattori P, Galletti C (2018)  
972 Uniformity and diversity of cortical projections to precuneate areas in the macaque  
973 monkey: what defines area PGm? *Cereb Cortex* 28:1700–1717.
- 974 Paxinos G, Huang X, Petrides M, Toga AW (2009) The rhesus monkey brain in stereotaxic  
975 coordinates (2 ed). San Diego, California, USA: Academic Press.
- 976 Rathelot JA, Strick PL (2009) Subdivisions of primary motor cortex based on cortico-  
977 motoneuronal cells. *Proc Natl Acad Sci USA* 106:918–923.
- 978 Rathelot JA, Dum RP, Strick PL (2017) Posterior Parietal Cortex Contains a Command  
979 Apparatus for Hand Movements. *Proc Natl Acad Sci USA*, 114:4255–4260.
- 980 Rossetti Y, Pisella L (2018) Optic ataxia: beyond the dorsal stream cliché. *Handb Clin Neurol*.  
981 151:225–247.
- 982 Rozzi S, Calzavara R, Belmalih A, Borra E, Gregoriou GG, Matelli M, Luppino G (2006) Cortical  
983 connections of the inferior parietal cortical convexity of the macaque monkey. *Cereb*  
984 *Cortex* 16:1389–1417.
- 985 Sabes PN (2011). Sensory integration for reaching: models of optimality in the context of  
986 behavior and the underlying neural circuits. *Prog Brain Res* 191:195–209.
- 987 Saleem KS and Logothetis NK (2012) A Combined MRI and Histology Atlas of the Rhesus  
988 Monkey Brain in Stereotaxic Coordinates (2 ed). London, UK: Elsevier Science.
- 989 Saleem KS, Miller B, Price JL. 2014. Subdivisions and connectional networks of the lateral  
990 prefrontal cortex in the macaque monkey. *J Comp Neurol*. 522:1641–1690
- 991 Schilling KG et al. (2019a) Limits to anatomical accuracy of diffusion tractography using  
992 modern approaches. *Neuroimage* 185:1–11.

- 993 Schilling KG, Gao Y, Stepniewska I, Janve V, Landman BA, Anderson AW (2019b) Anatomical  
994 accuracy of standard-practice tractography algorithms in the motor system - A  
995 histological validation in the squirrel monkey brain. *Magn Reson Imaging* 55:7–25.
- 996 Seehaus AK, Roebroek A, Chiry O, Kim DS, Ronen I, Bratzke H, Goebel R, Galuske RA (2013)  
997 Histological validation of DW-MRI tractography in human postmortem tissue. *Cereb*  
998 *Cortex* 23:442-50.
- 999 Seelke AM, Padberg JJ, Disbrow E, Purnell SM, Recanzone G, Krubitzer L (2012) Topographic  
1000 Maps within Brodmann's Area 5 of macaque monkeys. *Cereb Cortex* 22:1834–50.
- 1001 Strick PL, Kim CC (1978) Input to primate motor cortex from posterior parietal cortex (area  
1002 5). I. Demonstration by retrograde transport. *Brain Res* 157:325–30.
- 1003 Tanné-Gariépy J, Rouiller EM, Boussaoud D (2002) Parietal inputs to dorsal versus ventral  
1004 premotor areas in the macaque monkey: evidence for largely segregated visuomotor  
1005 pathways. *Exp Brain Res* 145:91–103.
- 1006 Thomas C, Ye FQ, Irfanoglu MO, Modi P, Saleem KS, Leopold DA, Pierpaoli C (2014)  
1007 Anatomical accuracy of brain connections derived from diffusion MRI tractography is  
1008 inherently limited. *Proc Natl Acad Sci USA* 111:16574-16579.
- 1009 Tournier JD, Smith R, Raffelt D, Tabbara R, Dhollander T, Pietsch M, Christiaens D, Jeurissen  
1010 B, Yeh CH, Connelly A (2019) MRtrix3: A fast, flexible and open software framework for  
1011 medical image processing and visualisation. *Neuroimage* 202:116137.
- 1012 van den Heuvel MP, de Reus MA, Feldman Barrett L, Scholtens LH, Coopmans FM, Schmidt R,  
1013 Preuss TM, Rilling JK, Li L (2015) Comparison of diffusion tractography and tract-tracing  
1014 measures of connectivity strength in rhesus macaque connectome. *Hum Brain*  
1015 *Mapp* 36:3064–3075.
- 1016 Van Essen DC, Jbabdi S, Sotiropoulos SN, Chen C, Dikranian K, Coalson T, Harwell J, Glasser  
1017 MF (2014) Mapping connections in humans and non-human primates: aspirations and  
1018 challenges for diffusion Imaging. *Diffusion MRI* 337–358.
- 1019 Youden WJ (1950) Index for rating diagnostic tests. *Cancer* 3:32–35.
- 1020 Zhang Y, Brady M, Smith S (2001) Segmentation of brain MR images through a hidden  
1021 Markov random field model and the expectation-maximization algorithm. *IEEE Trans Med*  
1022 *Imaging* 20:45–57.
- 1023

1024 **FIGURE LEGENDS**

1025

1026 **Figure 1.** Brain figurines in the top and middle left part of the figure and the corresponding  
1027 histological sections on the right show the location of the FB and DY injection sites along the  
1028 db-IPS (IPS) in Cases 72 and 73. Case 73 is shown as a right hemisphere. The IPS is shown as  
1029 “opened” to better visualize the dorsal and ventral banks. pPEip and aPEip indicate anterior  
1030 and posterior part of area PEip, respectively. The same applies to area MIP (aMIP, pMIP). In  
1031 the section drawings, the injection sites are shown as a deep colored zone corresponding to  
1032 the core surrounded by a light-colored zone corresponding to the halo. The bottom left part  
1033 of the figure shows a 3-D reconstruction of a right hemisphere in which the inferior parietal  
1034 lobule, including the ventral bank of the IPS was removed to show in a single comprehensive  
1035 image the relative antero-posterior locations of the four tracer injections (blue and yellow  
1036 spots) in the different parts of areas MIP and PEip. CS, STS, LS, PS, SAS/IAS, and CING indicate  
1037 central, superior temporal, lateral, principal, superior/inferior arcuate and cingulate sulci.

1038

1039 **Figure 2.** Distribution of RLC observed following HRP injections in the lateral funiculus of the  
1040 spinal cord at upper cervical levels in Cases 10 and 21, shown in dorsolateral views of the 3D  
1041 reconstructions of the injected hemispheres and lateral views of the db-IPS exposed after  
1042 dissections of the inferior parietal lobule and of part of temporal lobe. Each dot corresponds  
1043 to one labelled neuron. In the lower part of the figure coronal sections through C4 level of  
1044 the spinal cord show the HRP injection core (in red) and halo (in gray). Other abbreviations  
1045 as in Figure 1.

1046

1047 **Figure 3.** Distribution of RLC observed following tracer injections in the db-IPS, shown in  
1048 dorsolateral and mesial views of the injected hemispheres and in lateral views of the db-IPS.  
1049 The hemisphere of Case 73 is shown as a right hemisphere. Abbreviations and conventions  
1050 as in Figures 1 and 2; pre-CD indicates the precentral dimple.

1051

1052 **Fig. 4.** Distribution of retrogradely FB-labelled (blue) and DY-labelled cells (yellow) observed  
1053 in Case 72 after the tracer injections in aMIP and pPEip, respectively, shown in  
1054 representative sections through the frontal and the parietal cortex. The lightly colored zone  
1055 surrounding the injection site in sections 13 and 14 corresponds to a sector with  
1056 homogeneous intrinsic labeling. The levels at which the sections were taken is indicated in  
1057 the drawing of the hemisphere in the upper part of the figure. POS = parieto-occipital sulcus;  
1058 post-CD indicates post-central dimple. Other abbreviations as in Figures 1 and 2.

1059

1060 **Fig. 5.** Distribution of retrogradely FB-labelled (blue) and DY-labelled cells (yellow) observed  
1061 in Case 73 after the tracer injections in aPEip and pMIP, respectively, shown in relevant  
1062 sections through the frontal and the parietal cortex. Conventions and abbreviations as in  
1063 Figures 1,2 and 4.

1064

1065 **Figure 6. Ipsilateral cortical projections to areas aPEip, pPEip, aMIP, pMIP.** Proportion of  
1066 cells projecting from different areas to the four injection sites located in area aPEip (violet),  
1067 pPEip (orange), aMIP (blue), pMIP (green). pMIP cells projecting to PEip, and vice versa, are  
1068 included. Percentages are calculated relative to the total counts of RLC obtained after each  
1069 injection.

1070

1071 **Figure 7.** Gradient-like organization of the parietal and frontal projections to the dorsal bank  
1072 of the IPS. Mesial (top), lateral (bottom, right) and ventral (bottom, left) views of the monkey  
1073 brain showing the proportion of projecting cells (see Fig. 6) in their relative anatomical  
1074 location, after tracer injections (white ovals with colored arrows) at the four A-P levels of the  
1075 db-IPS. Each bar has a length proportional to the percent of RLC (range 1-30%, scale bar  
1076 corresponding to 5%) to aPEip (purple), pPEip (orange), aMIP (blue) and pMIP (green).  
1077 Conventions as in previous figures.

1078

1079 **Figure 8. A.** Pearson's correlation coefficient between the distribution of diffusion-based  
1080 connectivity estimated in 2.5 mm windows along the dorsal and middle sectors of the db-IPS  
1081 and the distribution of labelled cells after the four injection in aPEip, pPEip, aMIP, pMIP. MRI  
1082 slice numbers refer to the central position of each sliding window, where slice 103 is  
1083 anteriormost and slice 70 the posteriormost. The star markers indicate the A-P location with  
1084 the highest correlation coefficients. **B.** The Pearson's correlation coefficients after each of  
1085 the four injections are also reported in colour code across the db-IPS. Colour bar on the left.  
1086 In this image the rostralmost part of the db-IPS is not shown, since given its limited dorso-  
1087 ventral extent it could not be divided into three sectors.

1088

1089 **Figure 9.** Distribution of labelled cells and diffusion-based connectivity for locations with  
1090 maximum Pearson's correlation coefficients (aPEip:  $r=0.72$ ; pPEip:  $r=0.41$ ; aMIP:  $r=0.81$ ;  
1091 pMIP:  $r=0.66$ ). For each distribution, the MRI slices corresponding to the center positions of  
1092 the sliding windows with highest Pearson's correlation coefficients are reported next to the  
1093 reconstruction of the histological sections where the injection sites were found. The local  
1094 connections between MIP and PEip are not reported.

1095

1096 **Figure 10. A.** Pearson's correlation coefficient between the distributions of the diffusion-  
1097 based connectivity estimated in subregions along the db-IPS, as defined by a sliding window  
1098 of 2.5mm moving in the anterior-posterior direction (5 MRI coronal slices). For each window,  
1099 the connectivity is evaluated first by selecting all the streamlines connecting the MRI slices  
1100 to the 48 ROIs included in the analysis and summing the contribution to the intra-axonal MRI  
1101 signal fraction of each streamline for each cortical area. Data were normalized relative to the  
1102 total contribution of the streamlines associated to each sliding window. The X and Y axes  
1103 show the MRI slice number corresponding to centre position of each window. Star markers  
1104 (slices 99, 95, 88 and 78) indicate the locations with highest correlation coefficient between  
1105 diffusion-based connectivity and labelled cells, after tracer injections in aPEip, pPEip, aMIP,  
1106 and pMIP (see Fig. 8). Values of correlation coefficients are indicated by the colour code (see

1107 bar on the right). **B.** Pearson's correlation coefficients between the distributions of diffusion-  
1108 based connectivity estimated at the four sites reported above. **C.** Pearson's correlation  
1109 coefficients between the distributions of RLC after injection in aPEip, pPEip, aMIP, pMIP. In **B**  
1110 and **C** correlation coefficients are also reported with relative values (colour code as in **A**).  
1111

1112 **Figure 11.** Sum of the cortical connectivity of the db-IPS to other cortical ROIs. For each ROI,  
1113 the diffusion-based connectivity estimation is reported for the dorsal (red), middle (green)  
1114 and ventral (blue) sectors. The diffusion connectivity corresponds to the sum of streamline  
1115 contributions to the intra-axonal MRI signal fraction estimated using COMMIT for each  
1116 cortical ROI. The sectors of the db-IPS are shown on the mid cortical surface (top right) and  
1117 on the db-IPS (bottom right). Notice that the rostralmost part of the db-IPS (grey region) was  
1118 not used for this analysis, since it could not be parcellated into three D-V sectors, given its  
1119 limited extent in the D-V dimension).

1120  
1121 **Figure 12.** Spatial distribution of the IPS connectivity estimated from DW-MRI along 34  
1122 dorsal, middle and ventral anterior-posterior sectors of the db-IPS, for the 12 cortical ROIs  
1123 displaying the strongest estimated connectivity with the db-IPS (see Fig. 11). The figure  
1124 shows a three-dimensional rendering of the IPS, with the yellow and orange highlighting the  
1125 IPS locations with the strongest estimated connectivity for the corresponding cortical areas.  
1126

1127  
1128 **Table 1.** Distribution (%) and total number (n) of labelled neurons observed after tracer  
1129 injections in MIP and PEip. Injection sites are sorted relative to their antero-posterior  
1130 position along the db-IPS, to better display the gradient-like distribution of their projections  
1131 (–, labelling < 0,1 % or no labelling). No cell counts are reported for the areas containing the  
1132 injection sites (**X**).

1133  
1134

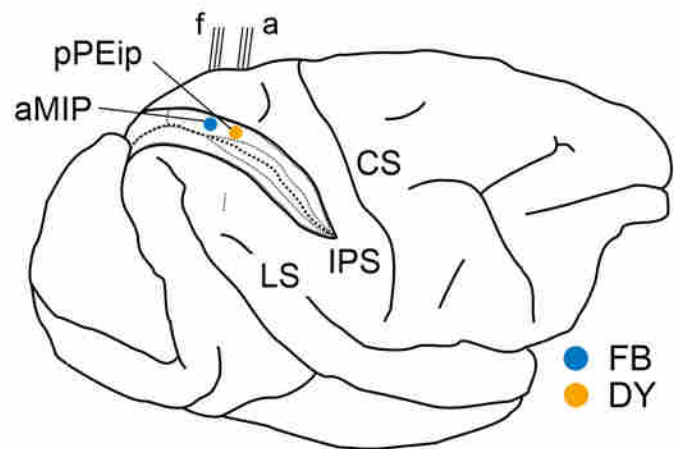
1135 **TABLE 1**

1136

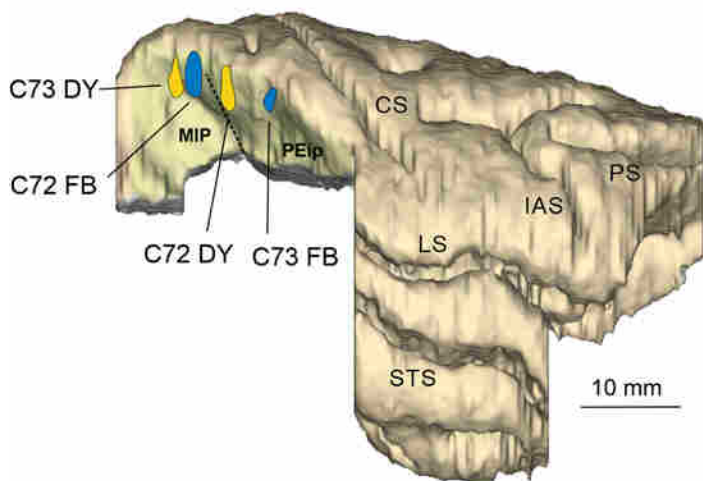
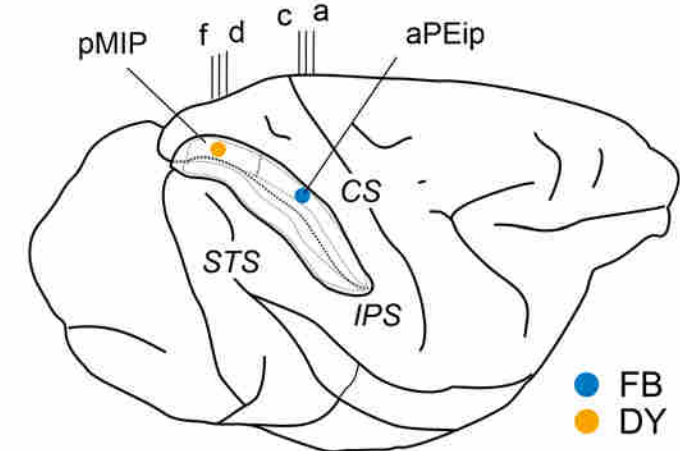
<b>Injected area</b>	<b>aPEip</b>	<b>pPEip</b>	<b>aMIP</b>	<b>pMIP</b>
Case	73FB	72DY	72FB	73DY
<i>Prefrontal</i>				
12r, 12l, 12m&12o, 11m&11l, 13,GrFO, 10, 31, 32, 24, 25, 14, 9, 45A&B, 46d, 46v, 8B, 8r&FEF	-	-	-	-
<i>Frontal</i>				
F6	-	0,2	-	-
F7	-	0,3	0,1	-
F3	1,4	4,9	1,6	1,3
F2	1,2	13,4	10,9	10,2
F5	1,5	0,7	0,2	0,5
F4	5,0	2,9	-	0,2
M1 (F1)	15,6	13,5	3,8	3,7
<i>Cingulate</i>				
24c&d	3,7	3,0	2,7	2,0
24a&b	-	0,2	0,1	0,3
23a&b	-	-	-	-
23c	3,7	1,6	1,2	2,3
<i>Somatosensory</i>				
SI	7,3	-	-	-
SII	1,6	0,2	-	-
<i>Insular</i>				
	1,7	-	-	-
<i>Superior parietal (SPL)</i>				
PE	18,3	11,1	17,8	4,1
PEc	1,1	4,2	18,2	12,5
PEci	2,2	5,3	6,1	12,9
PGm	-	1,6	7,1	0,7
V6A	0,7	10,5	7,3	22,2
<i>Intraparietal (IPS)</i>				
PEip	<b>X</b>	<b>X</b>	13,8	16,5
MIP	5,1	12,9	<b>X</b>	<b>X</b>
AIP	6,3	0,5	-	0,2
VIP	5,5	2	0,7	1,3
LIP	-	-	-	-
<i>Inferior parietal (IPL)</i>				
PF	0,7	-	-	-
PFG	3,8	2,4	1,1	0,8
PG	0,7	3,4	3,6	4,3
Opt	-	-	-	-
PGop	11,7	4,2	2,8	3,9
<i>Temporal</i>				
MST	1	0,8	0,7	-
MT	-	-	-	-
Tpt	0,2	-	0,1	-
<b>N° labelled cells</b>	<b>20556</b>	<b>62312</b>	<b>21927</b>	<b>61135</b>

1137

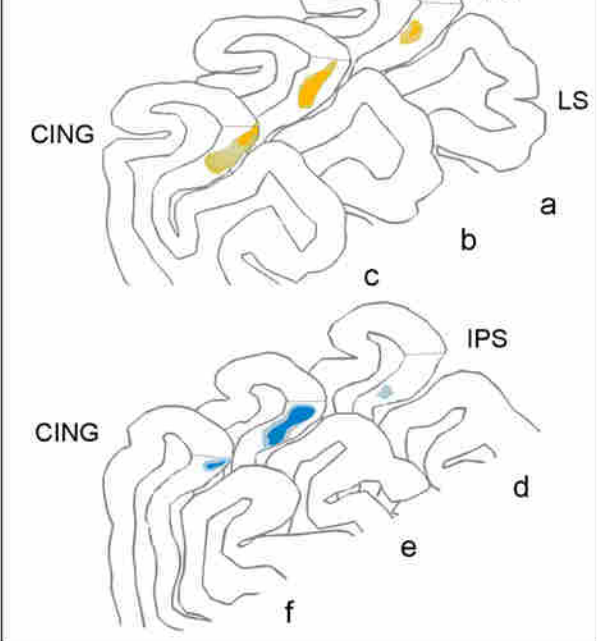
### Case 72



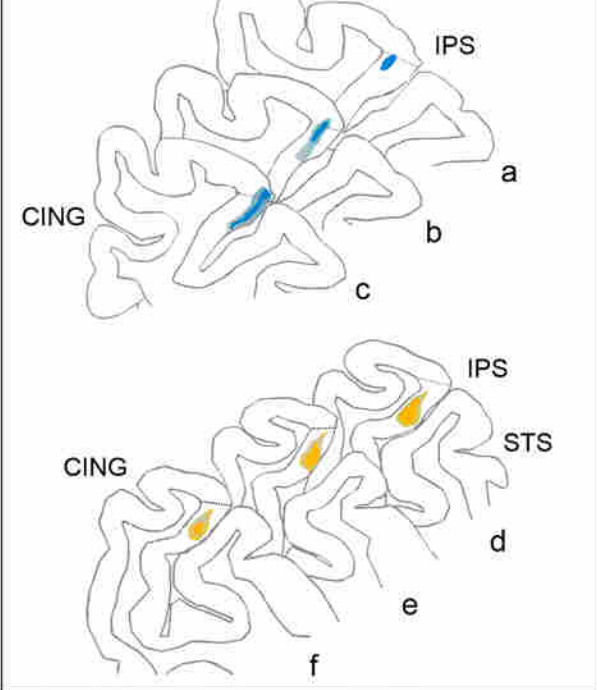
### Case 73

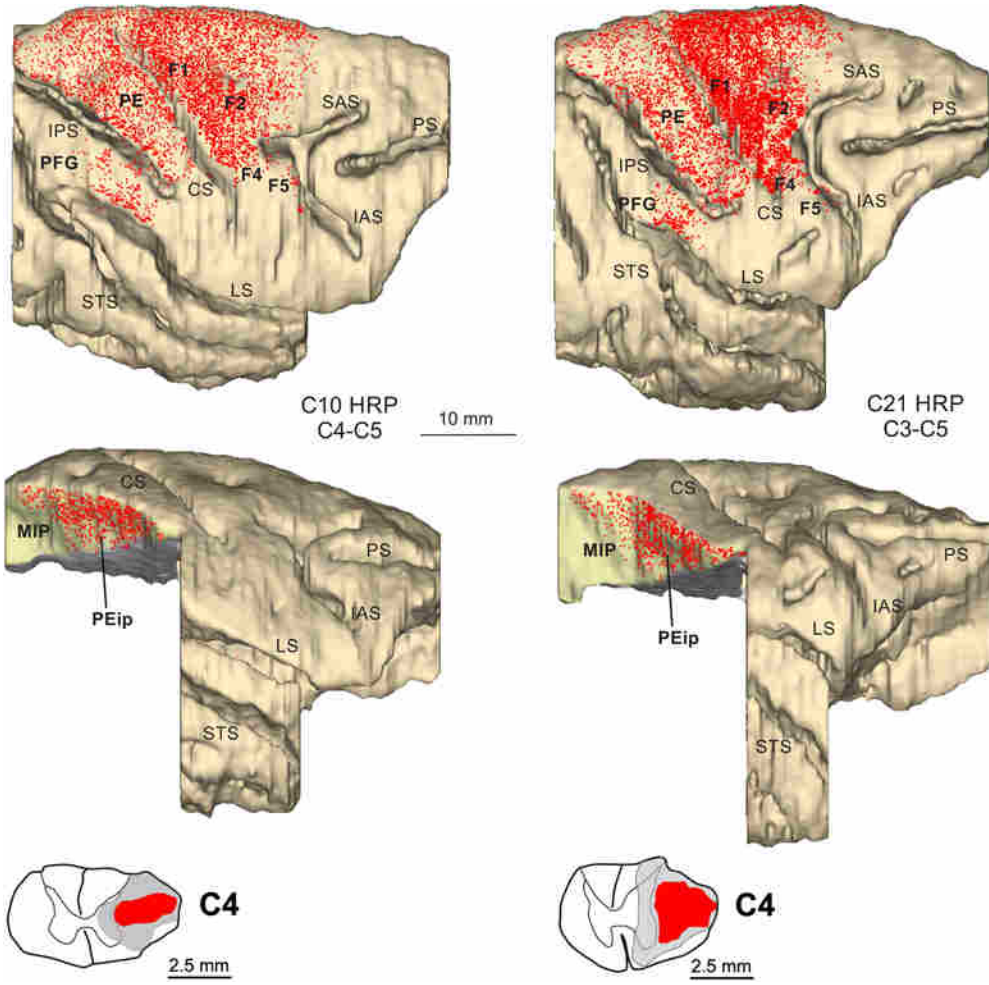


### Case 72

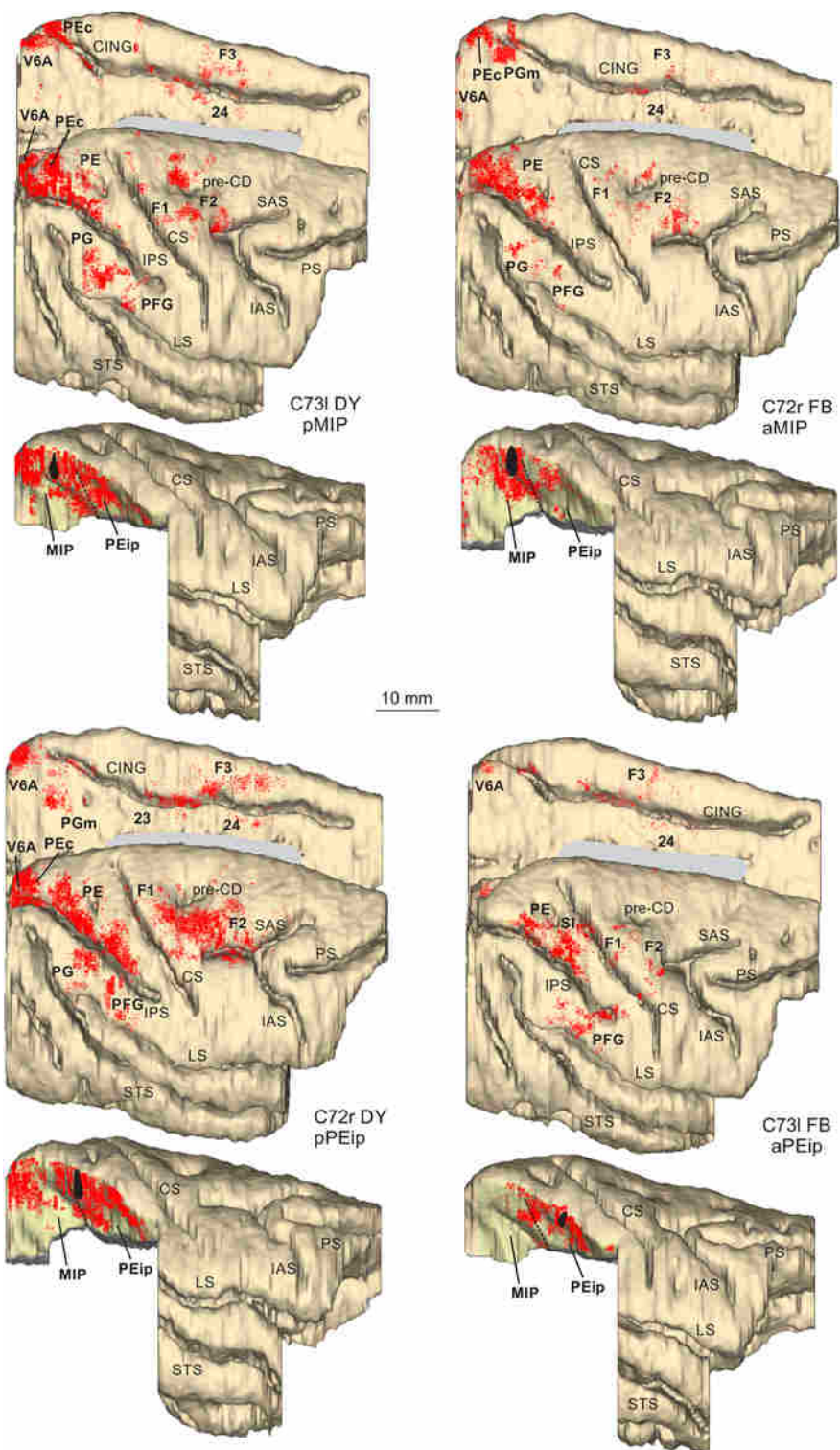


### Case 73

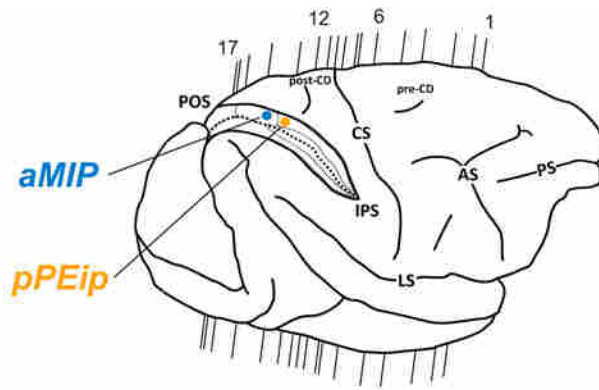




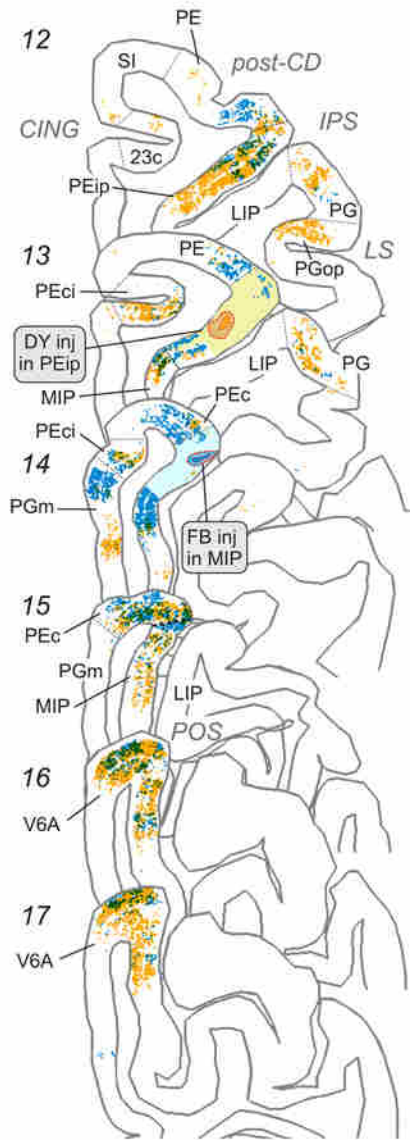
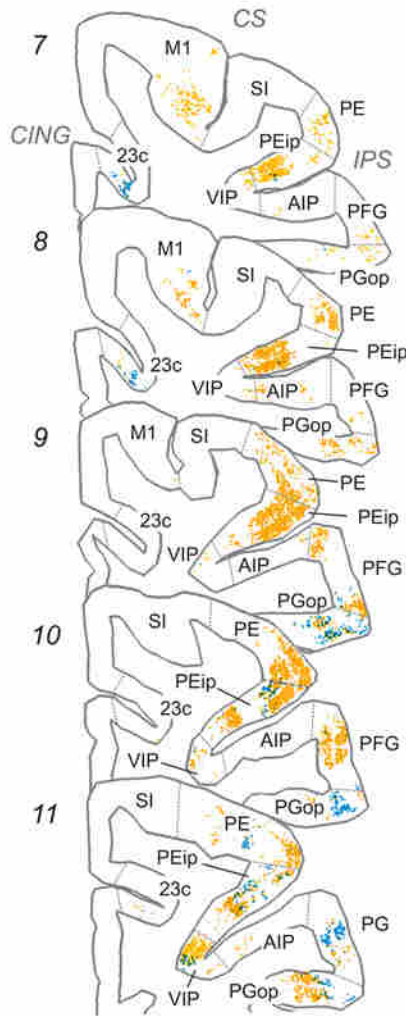
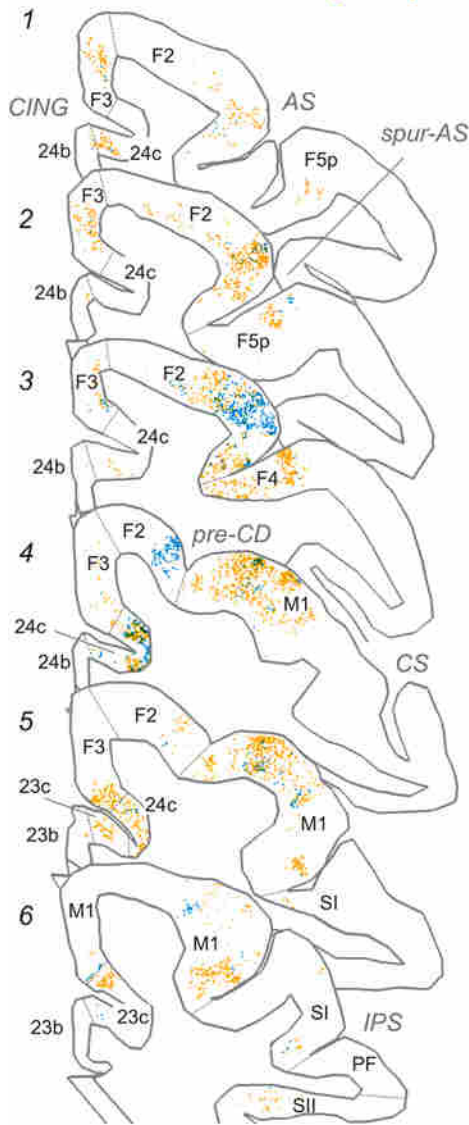




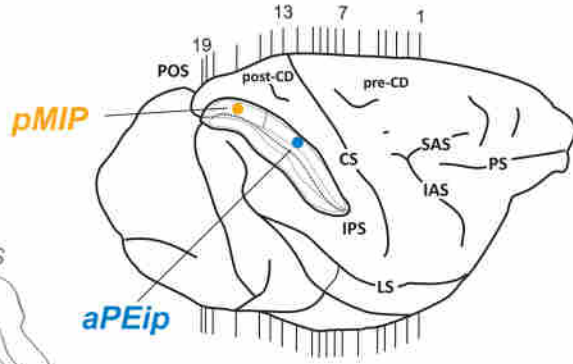
case 72



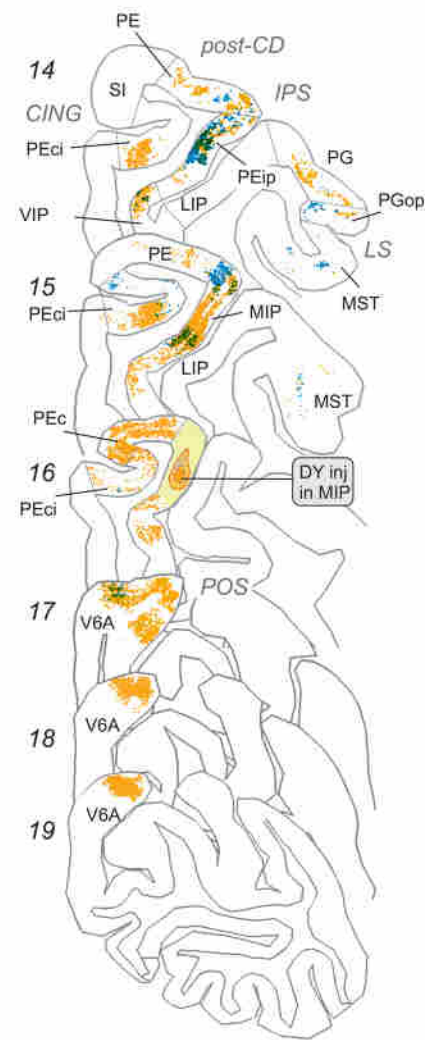
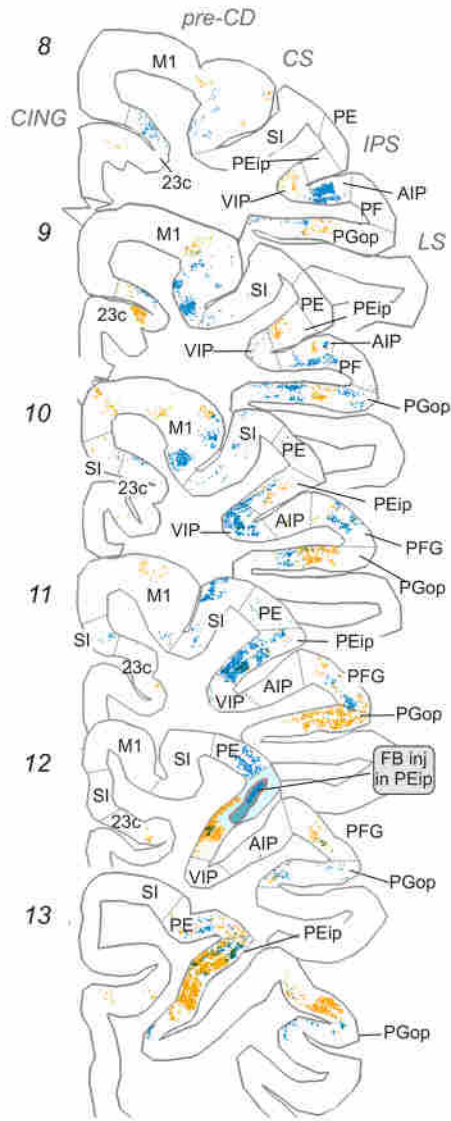
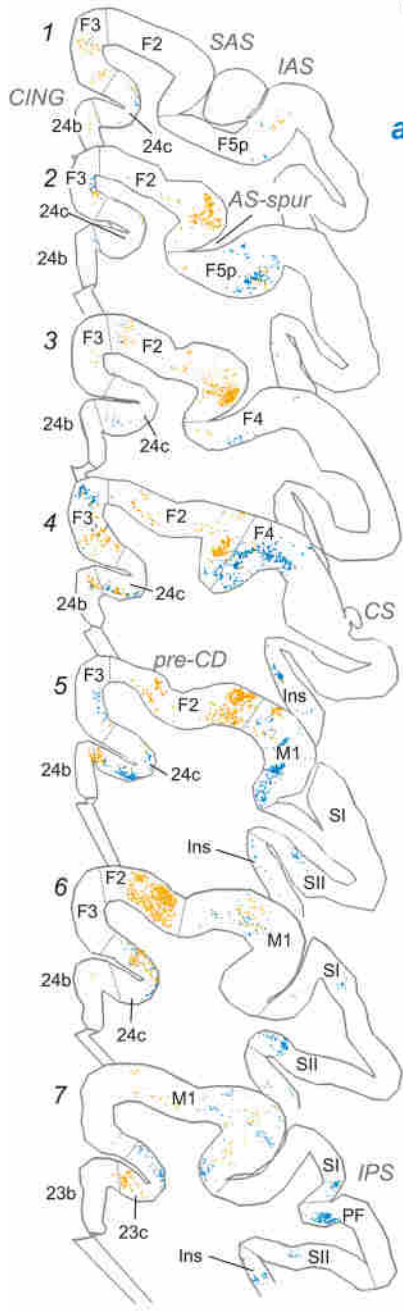
● DY  
● FB

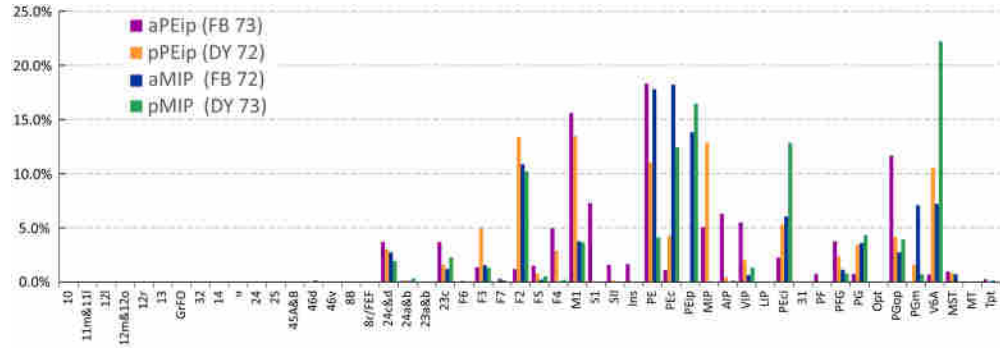


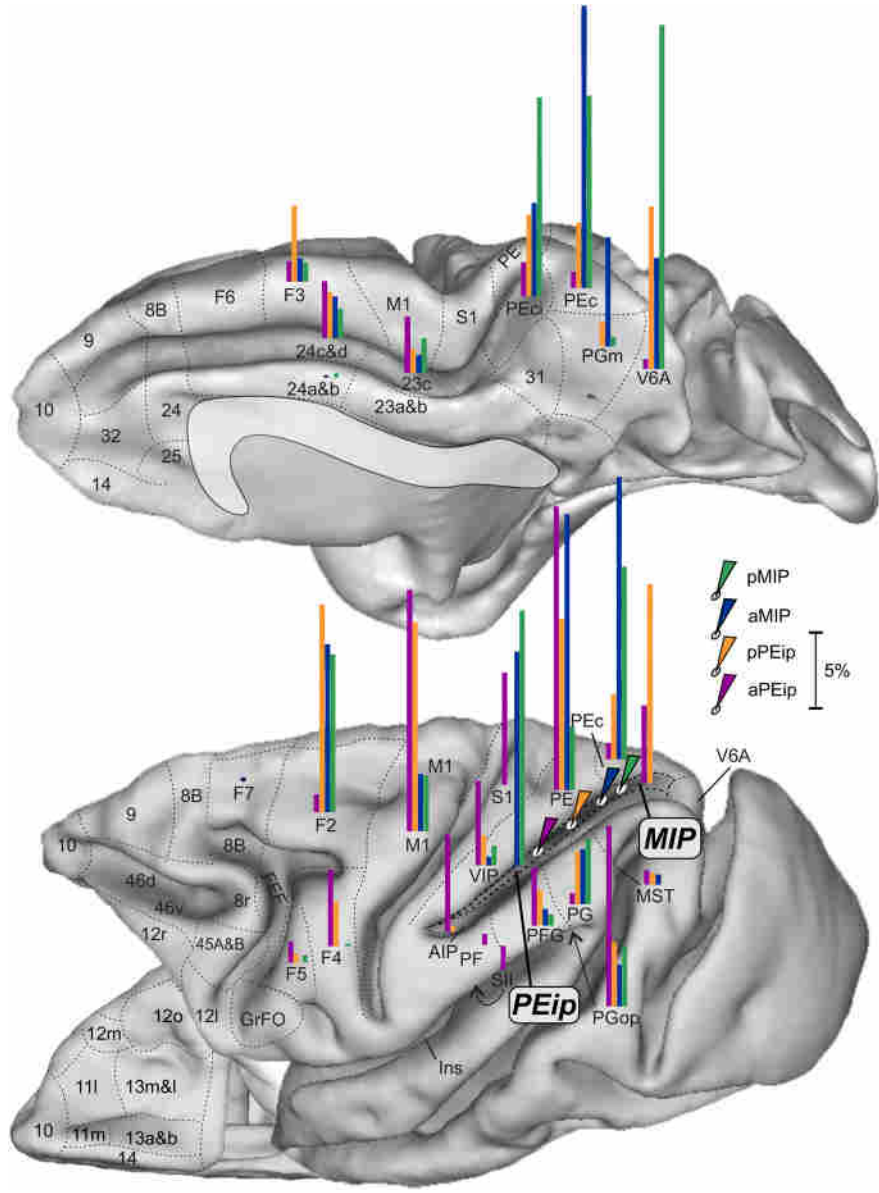
case 73

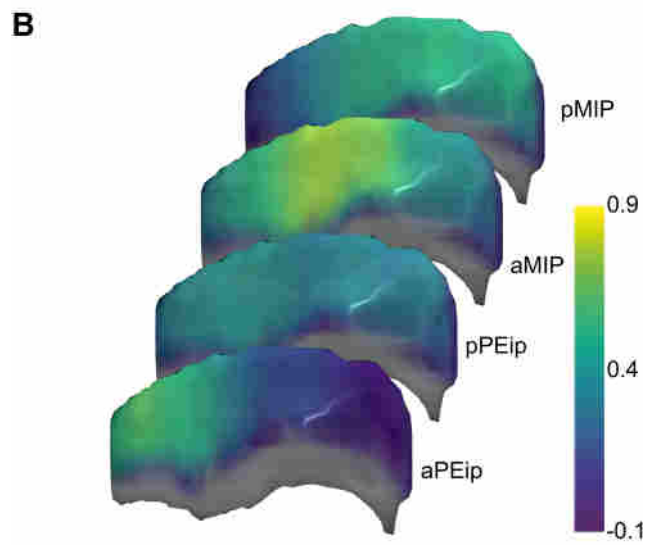
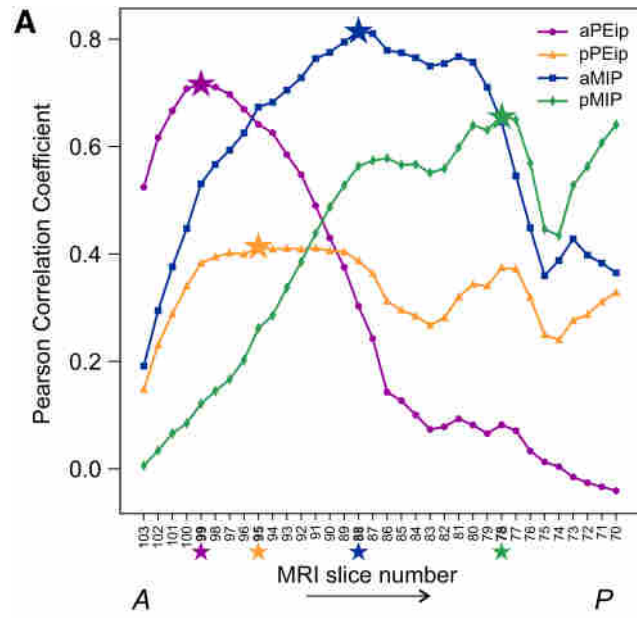


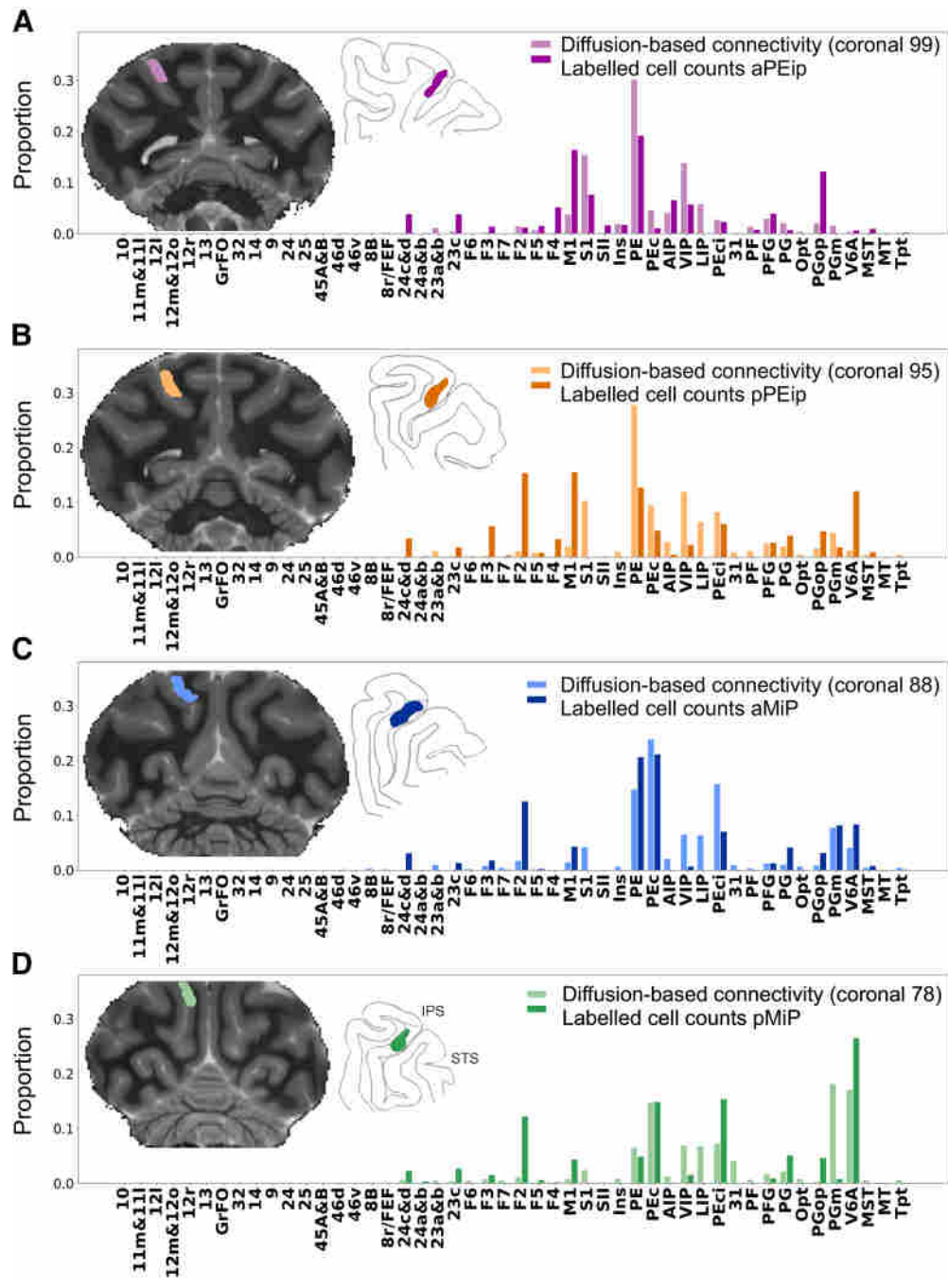
● DY  
● FB

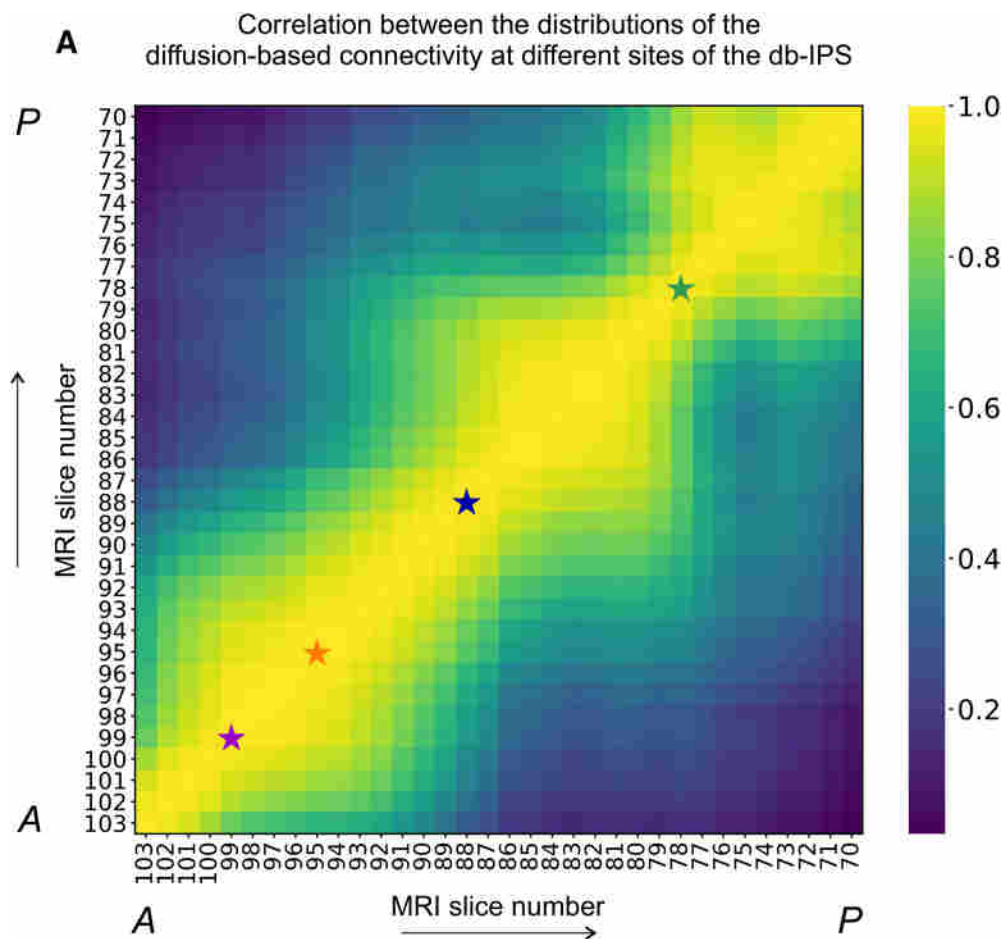












**B** Diffusion-based connectivity

pMIP	0.30	0.47	0.73	1
aMIP	0.56	0.75	1	0.73
pPEip	0.96	1	0.75	0.47
aPEip	1	0.96	0.56	0.30
	aPEip	pPEip	aMIP	pMIP

**C** Retrograde Tracer connectivity

pMIP	0.15	0.70	0.67	1
aMIP	0.43	0.71	1	0.67
pPEip	0.61	1	0.71	0.70
aPEip	1	0.61	0.43	0.15
	aPEip	pPEip	aMIP	pMIP



